Vacuum Brazing of
Carbon Nanotube Strands

by

Wei Wu

A thesis
presented to the University of Waterloo
in fulfilment of the
thesis requirement for the degree of
Master of Applied Science
in
Mechanical Engineering

Waterloo, Ontario, Canada, 2009

Declaration

I hereby declare that I am the sole author of this thesis. This is a true copy of the thesis, including any required final revisions, as accepted by my examiners.

I understand that my thesis may be made electronically available to the public.

_____
Wei Wu

Abstract

Carbon nanotubes (CNTs) discovered at 1991 have attracted great interest for applications in Nano-Electro-Mechanical-Systems (NEMS). However, the search for methods to join CNTs with metallic parts has been a worldwide challenge. Many efforts have been devoted to manipulating individual CNTs and joining them to each other. Joining processes so far attempted are premature and fall short of efficiency for joint quality evaluation. Thus, it has been found necessary to work on macro CNTs strands which are easy to handle *via* macro joining techniques. In this study, vacuum brazing technology has been developed for joining macro CNTs strands with Ni using a Ti-Ag-Cu alloy. The brazing mechanism has been confirmed as due to TiC formation at the CNTs/Ti-Ag-Cu interface.

To evaluate this novel vacuum brazing technique for CNTs joining, the temperature effect on the brazing mechanism, microstructure and stoichiometry at joint interface needed to be understood. Firstly, the influence of temperature (from room temperature to 1000°C) on mechanical behaviour of CNTs was well examined. The ultimate tensile strength (UTS) of CNTs was measured to be a maximum at 900°C.

Then, the mechanical performance of the joints was investigated from 850°C to 1000°C, and the fracture modes of the joints were identified. The UTS of joint also achieves maximum at 900°C. Below 900°C, due to little TiC formation, the bonding is weak thus leading to interfacial fracture. Above 900°C, due to much TiC formation, the bonding is strong thus resulting in CNTs fracture.

Furthermore, the vacuum brazing technique was applied to join CNTs to Ni contact wires used as a lamp filament. Compared to the filament joined by Ag paste or mechanical connection, the illumination of the brazed CNTs filament was stronger. The current density of the brazed filament was superior to the Ag paste connected filament. This may represent a promising way to produce energy saving lamps.

Acknowledgements

Dedication

I wish to dedicate this thesis to my parents Dongshui Wu, Guixin Ma and my husband Xiulei Ji. Without my parents' support, I would have struggled financially throughout my undergraduate studies, and likely would not have been in a position to undertake the challenge of a master degree. Discussions with them regarding my research helped me focus on the immediate tasks and overall goals, and motivated me to do what needed to get done.

Table of contents

List of Figures

List of Tables

Chapter 1

Introduction

In today's electronic industry, electronic devices are becoming smaller in size, which requires smaller wires, thus smaller interconnects. Traditional metal wires experience quantum conducting effects as size becomes extremely small. Novel materials are then required as electronic wires. Carbon nanotubes (CNTs) discovered by Sumio Iijima in 1991 [1] are advanced materials with exceptional advantageous characteristics, such as high conductivity, high hardness and high Young's modulus, which make them ideal candidates as constitutive elements in Nano-Electro-Mechanical-Systems (NEMS), such as nanomotors, switches, rectifiers, field-effect transistors and high frequency oscillators [2].

1.1   Motivation

Difficulty in reproducible fabrication of joints between CNTs and other conductors has been identified as a major impediment to realizing electronic applications of CNTs including quantum wires, ballistic conductors, microchip interconnects and transistors. Previous studies have shown that electrically conductive connection between nano-building-blocks is not straightforward. Instead of desirable ohmic contacts, tunnel junctions or weak links for contact regimes on the order of 1 nm^2 often generate a high contact resistance, typically 200 kΩ, [3]. Normally, the gap-sensitive contact resistance makes it difficult to join nano-building-blocks with repeatable performance in nanodevices.

Similar to other ceramic/metal joining, CNTs/metal joining encounters similar difficulties such as dissimilar types of atomic bonding, mismatched lattice parameters and thermal

expansion coefficients. Furthermore, extremely small dimensions of CNTs lead to great difficulty in manipulation of the work pieces, thus making the joining of CNTs very complex. This has been partially resolved with recently produced centimetre long CNTs strands (ie, macro bundles of many CNTs) [4]. Thus the current question is to develop an appropriate joining technique for the strands.

As a well established method in ceramic/metal joining, brazing can be used to introduce an intermediate filler metal to realize bonding between ceramic and metal. Ceramics are typically assembled by strong covalent bonds. Thus, to join a metallic material to a ceramic, an active element in the brazing alloy is highly necessary to react with the ceramic. Elements including Ti, Zr, Cr, Hf, V, Ta and Al can form e.g. carbides or nitrides at the ceramic/metal interface and thus modify the ceramic surfaces to metalloids which are directly wettable by the metallic brazing alloy. Particularly, chromium and titanium are the most effective elements to enable the wetting of carbon materials [5].

Prior to the work reported here, the applicability of a macro brazing technique for nanojoining of CNTs was unknown. Further unanswered questions included identification of the key brazing parameters such as temperature, atmosphere, and the ways in which brazing parameters affect the joint quality.

1.2   Objective

The objective of this research was four-fold. The first objective was to realize the successful joining of CNTs to Ni through the vacuum brazing technique [6] which is typically capable of joining dissimilar materials.   Herein, CNTs and Ni have been bonded through a

brazing alloy (Ag_xCu_y) doped with Ti, a reactive transition element usually added to brazing alloys to aid the brazing under vacuum conditions or in protective atmosphere. The second objective was to investigate and determine the effect of brazing temperature on the mechanical performance and microstructure of both CNTs and CNTs joints. The third was the failure analysis of CNTs material and the brazing mechanism analysis of CNTs joint based on the mechanical and microstructure investigation and the stoichiometry measurement at the joint. The last was to study the application of vacuum brazed CNTs in energy saving lamps.

1.3   Thesis Outline

A study of previous research including CNTs mechanical properties, CNTs vacuum brazing theory and CNT/Ni joint mechanism has been carried out. The basic ceramic/metal brazing theory is described in **Chapter 2**. Review of CNTs properties, CNT joining methods, as well as joint quality evaluation is also discussed in this section. The experimental procedures are presented in **Chapter 3**. **Chapter 4** presents creative application of conventional macro ceramic brazing theory to CNTs/Ni nano-brazing process. Then the brazing mechanism is discussed in **Chapter 4** as well. The temperature effects on microstructure, mechanical performance of both CNTs and CNTs joint from room temperature to 1000°C are reported in **Chapter 5**. Finally, in **Chapter 6**, a practical application of developed nano-brazing technique is tried and compared with the results obtained by other groups. Conclusions for this thesis are drawn in **Chapter 7**.

Chapter 2

Literature Review

2.1 Overview of CNTs

After the discovery and verification of fullerenes in 1985 [7], Sumio Iijima at NEC (Nippon Electric Company) observed multiwall carbon nanotubes (MWCNTs) formed in a carbon arc discharge in 1991 [1]. Two years later, he and Donald Bethune at IBM observed single-wall nanotubes (SWCNTs) independently [8]. Different from graphite which is composed of parallel graphene layers, CNTs comprise hexagonal C rings with pentagonal faces plus various amounts of hexagonal faces at each end of the tubes. It is well known that MWCNTs are invariably produced with a high frequency of structural defects which inevitably degrade their mechanical properties. Nevertheless, compared with their larger counterparts, 5-20 µm long graphite fibres, they are still quite structurally sound due to the molecular invariance. The molecular invariance of CNTs is a critically advantageous feature, compared with their larger defective cousins such as graphite, diamond, due to the fact that every atom in the right place results in a stable structure.

The atomic structure of CNTs is described in terms of the tube chirality or helicity, defined by the chiral vector, $\overrightarrow{C_h}$, and the chiral angle, θ. As shown in **Figure 2.1**, the CNTs as cutting the graphite sheet along the dotted lines and rolling the tube so that the tip of the chiral vector touches its tail. The chiral vector could be expressed in the following equation [9],

$$\overrightarrow{C_h} = n\overrightarrow{a_1} + m\overrightarrow{a_2} \qquad (2\text{-}1)$$

where n, m are the number of steps along the zig-zag of carbon bonds of the hexagonal lattice, $\vec{a_1}$, $\vec{a_2}$ are unit vectors. The chirality can also give information on the diameter of the tube since the atomic spacing of graphite is known.
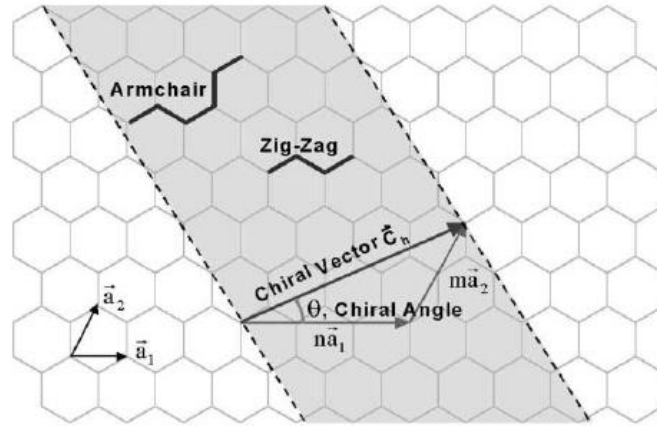
Figure 2.1 Schematic diagram showing the process of cutting a graphite layer and rolling it into a carbon nanotube [9].

2.1.1 Microstructure characterization

The microstructure of the CNTs strands has been investigated by other groups. Zhu et al. were the first group in the world to produce centimetres long CNTs strands [10]. MWCNTs, DWCNTs, SWCNTs strands they fabricated are shown in **Figure 2.2** [11,12]. As seen in **Figure 2.2b**, in each macrosized strand, there are thousands of individual CNTs entangled together through van der Waals force without perfect alignment. HRTEM examination (**Figure 2.2c,d,f**), showed that each DWCNTs has inner and outer diameter around 3 and 3.5 nm, respectively, and the tube diameter of each SWCNT is around 1nm. The SEM microstructure (**Figure 2.2e**) of the strands revealed a web like configuration in each strand, which indicates complex mechanical performance of the macro strands.
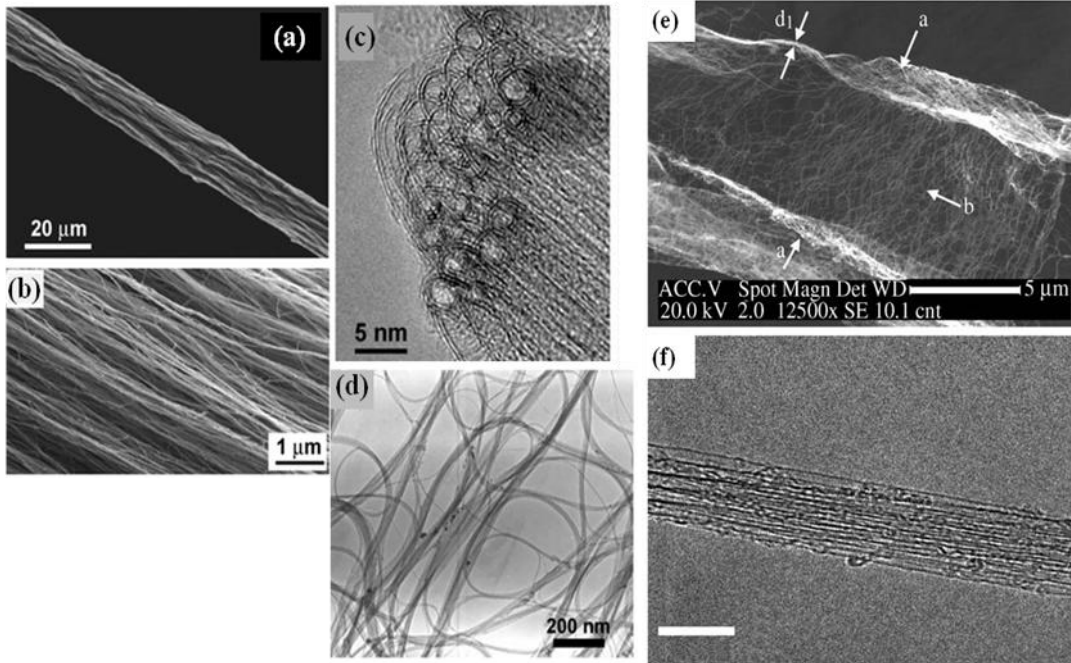
Figure 2.2 Microstructure of MWCNTs, DWCNTs bundles and SWCNTs bundles. (a),(b) low and higher magnification SEM of aligned nanotube in MWCNTs bundles with 20 μm width; (c) High resolution TEM image of DWCNTs tube along its axis direction; (d) TEM image of as-grown DWCNTs displaying very low level of catalyst particles in the same sample; (e) SEM image of the SWCNTs film; (f) HRTEM image of the SWCNTs with scale bar 10nm. [11,12]

2.1.2 Mechanical properties

Due to the nano-scale size of individual CNTs, it is hard to directly measure their mechanical properties although atomic force microscope can be employed for estimation purposes. Indirect methods such as theoretical calculation are normally utilized to determine the mechanical properties. However, for macro strands of CNTs, due to their macro scale size, strength could be measured on tensile testing apparatus.

Zhu et al. [13] performed tensile tests on the well aligned SWCNTs strands and obtained a maximum tensile strength of 1.2 GPa. Then the individual CNT's Young's Modulus was

6

reported as 48~77 GPa based on calculation. Considering the volume fraction of CNTs in the strands, the true tensile strength could be 2.4 GPa, then the Young's Modulus could reach 100~150 GPa, very close to the theoretical prediction. Li et al. [14] performed tensile tests on well aligned DWCNTs strands and obtained an average tensile strength and the Young's Modulus of 1.2 GPa and 16 GPa, respectively.

Reported by Gu et al. [15], the mechanical properties of DWCNTs membrane were measured and compared with various forms of CNTs. The curves in **Figure 2.3**, suggest that the membranes experience two processes (A-B and B-C) during the tensile loading until their fracture as indicated in the stress vs. strain curve. When the DWCNTs membrane is under load, the stress increases linearly with the strain. The region A-B of the curve is regarded as the elastic deformation region. In the region B-C, the slope decreases gradually as the stress increases. This is defined as the plastic deformation region. The stress increases slowly until the membrane breaks at the top point C, where the ultimate tensile strength (UTS) and maximum elongation are obtained. The elastic region is due to the elastic elongation of the CNT itself, the plastic region is due to the slippage between the CNT tubes and the intrinsic non linear behaviour of the CNT tubes themselves. The schematic to describe this process is shown in **Figure 2.4**. They have compared their results with the currently available data listed in **Table 2.1**. As shown in **Table 2.1**, the CNTs entangled together in a film or membrane form have comparatively lower tensile strength than the CNTs strands. This is understandable since the tensile strength of the CNTs macro-strands or films is a reflection of the van der Waals force within the materials which depends on the compactness of the bundles. A CNTs macro-strand is much denser than a CNTs film. Interestingly, the Young's modulus of DWCNTs films and strands were shown to be lower than that of SWCNTs films and strands. This can be explained by the double layer of hexagonal

7

carbon configuration in DWCNTs which are weakly bonded via the van der Waals force. This indicates that their theoretical mechanical strength should be lower than the estimated value of individual SWCNTs strands or films. Since Young's modulus represents the intrinsic character of a certain material, it is reasonable to expect SWCNTs films and strands to have comparable Young's modulus and similarly with the DWCNTs films and strands.
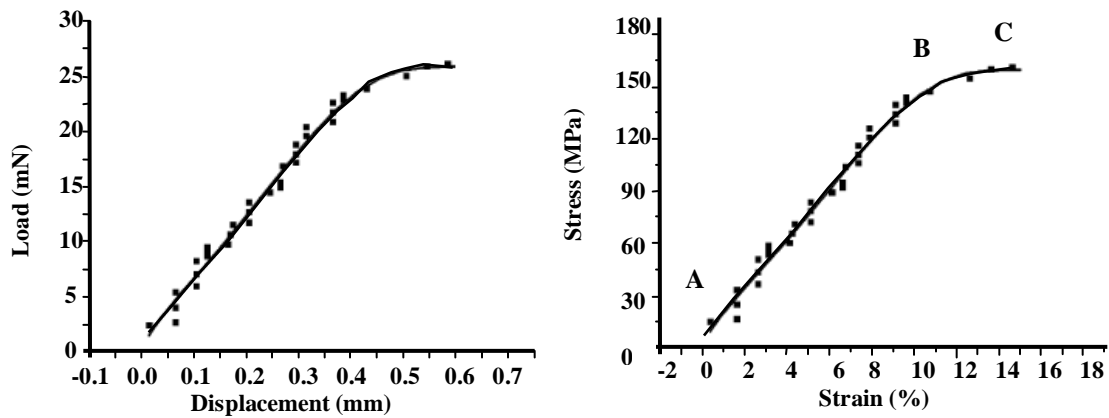
Figure 2.3 (a) Typical curve of load vs. displacement; (b) Typical curve of stress vs strain for one sample of DWCNTs membrane. [15]
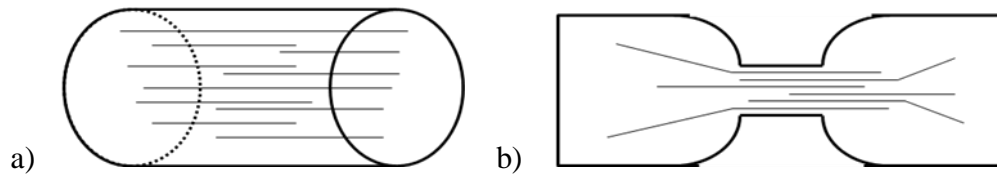
Figure 2.4 Schematic drawing shows (a) before tensile stress loading; (b) top view of the CNTs strands during stress loading.

Table 2.1 Comparison of currently available tensile data

Authors	Objects	Strength (MPa)	Young's Modulus (GPa)
Zhu et al.[10]	SWCNTs strands	~1000	49-77
Li et al.[16]	DWCNTs strands	1200	16
Ericson et al.[17]	SWCNTs yarns	116$\pm$10	120$\pm$10
Song et al.[18]	SWCNTs films	400$\pm$154	500$\pm$190
Zhang et al.[19]	SWCNTs films	74	5
Gu et al.[15]	DWCNTs	640	7.2

2.1.3 Electronic properties

The electronic structure of CNTs largely depends on the chiral vector $\overrightarrow{C_h}$, chiral angle θ, and the diameter of the tube. Saito et al. [20] have observed that 1/3 of the tubes were metallic and 2/3 of the tubes were semi-conducting, although there was no difference in local chemical bonding of carbon atoms and no impurities included. Furthermore, the energy band gap for the semi-conducting tubes decreased with increasing tube diameter. In 1998, Wildöer et al. related the electronic structure of single CNTs to their chirality and chiral angle by using Scanning Tunnelling Microscope (STM) for the first time [21]. They discovered that a small variation in tube diameter and chiral angle leads to the transformation from metallic tube to semi-conducting tube, which is in good consistency with the theoretical predictions made previously.

Thess et al. reported a direct experimental method to measure the resistivity of a SWCNTs rope by using the four probe technique [22]. The SWCNTs rope they measured had a resistivity ranging from 0.34 to 1.0×10^{-4} $\mu\Omega\cdot$cm. Ebbesen et al. also measured the resistance of SWCNTs by using the four-probe technique, and determined that it varied from tube to tube [23]. Both tube structure defects and the tube temperature when conducting affected the resistance

significantly. Generally, SWCNTs should exhibit considerably less resistivity than MWCNTs since the tube-tube resistivity in MWCNTs is quite large due to the weak molecular bonding. Kociak et al. connected the ropes of SWCNTs with nonsuperconducting metallic pads and measured the resistance [24]. They concluded that when temperature is below 0.55K, the resistance of the rope drops by 2 orders of magnitude, which will not occur under a magnetic field larger than 1 T or a D.C current greater than 2.5μA. This suggests some superconductivity behaviour of SWCNTs ropes. Furthermore, Tang et al. measured the superconductivity transition temperature of SWCNTs with a diameter of 4 Å to be 15K through TEM, higher than any existing single element materials [25].

2.1.4 Other properties

Besides their unusual mechanical and electronic properties, other advantageous properties of CNTs have also been reported. Berber et al. have combined the results of equilibrium/non-equilibrium molecular dynamics simulations and exact carbon potentials to determine the thermal conductivity of an isolated (10, 10) SWCNTs to be 6000W/mK [26]. It is believed that this high value is due to the long phonon mean free path in CNTs. The numerical data indicates that the thermal conductivity will be dramatically reduced in graphite due to the existence of interlayer coupling.

Ajayan and Iijima discovered an experimental phenomenon where annealing of the CNTs in the presence of liquid lead resulted in the opening of the capped tube ends and filling of the CNTs with molten lead by capillary force [27]. It suggests the potential of producing nano metallic wires or composites.

Wang et al. have measured room temperature susceptibility of CNTs to be -10×10^{-6} emu/g, for the magnetic field parallel to the tube axis [28]. This is about 30 times larger than C_{60}, and probably the largest in the fullerene family due to delocalized electrons in the graphene sheet.

Kataura et al. have observed the optical spectra of SWCNTs and found that it was in good consistency with the calculated values [29]. Even the mixture ratios of the semi-conducting to metallic CNTs could be estimated from the spectra.

2.1.5 Defect analysis

CNTs have structural defects in their honey comb like structure, which will affect their performance in applications. Existence of SWCNTs intermolecular junctions has been suggested by theoretical calculations [30] and experiments [31], which results from the Pentagon-heptagon pair defects. Similar to bulk materials, defects in CNTs can be removed by high temperature annealing. Tsai et al. discovered a rapid thermal annealing process using a DC vacuum arc discharge system to reduce defects in carbon nanotubes (CNTs) [32]. MWCNTs exhibit high-density structural imperfections if they are deposited via chemical vapour deposition at relatively low temperatures (e.g. 650°C). These defects can be thermally annealed to reconstruct the graphitic structure, as shown in **Figure 2.5**. A vacuum arc discharge system was used to anneal the MWCNTs through several cycles at high temperatures (1800°C) followed by a rapid cooling. Gong et al. also reported the effectiveness of the heat treatment (from 1800 °C to 3000°C) for the well aligned carbon nanotubes [33]. Some impurities could be removed once the annealing temperature exceeded the vaporization point of a corresponding metal or non-metal catalyst imbedded in the CNTs. Desorption of oxygen could be attributed to reduced active sites of dangling covalent bonds after a heat treatment. After annealing, the amorphous carbon originally

11

sticking to the periphery of the outer wall of CNTs is reconstructed into tubular graphitic layers. It was suggested by Gong et al. that heat treatment would be a necessary process to remove residual catalysts, other impurities and structural defects in CNTs.
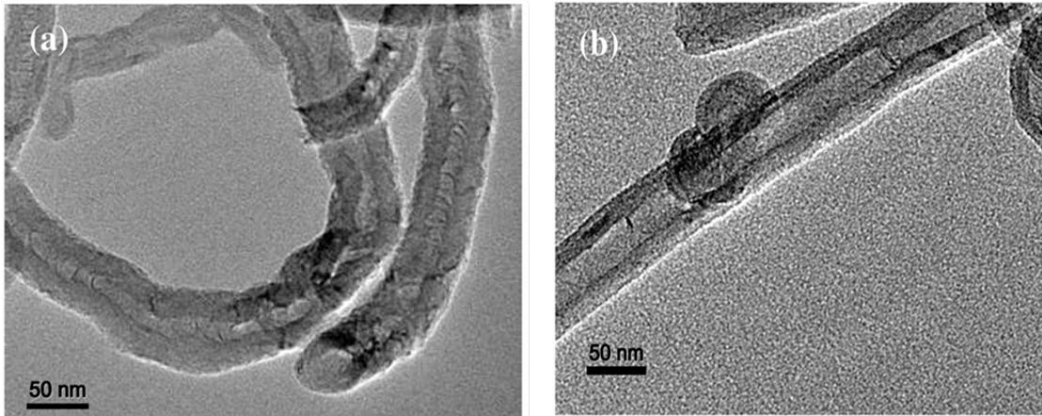
Figure 2.5 (a) TEM micrograph of the as-grown MWCNTs from MWCVD reactor; (b) after optimum rapid annealing process, the defects have been reduced. [32]

2.2 Joining of CNTs

Various methods of joining CNTs to each other or to other metals have been attempted by several groups. These methods include welding, soldering and gluing to achieve electronic interconnections. As the object size goes down to the nanometer scale, the joining mechanisms can be classified into two chemical bonding types: joining through primary force and joining through secondary force. Joining through primary force refers to the formation of primary atomic bonding; while joining through secondary force refers to the formation of molecular bonding.

2.2.1 Joining through primary force

Joining by definition is to connect two parts together. There are two approaches to produce a junction. One could either join two separate building blocks by using exterior energy sources, or directly grow the desired junction from substrates.

To overcome the energy barrier existing between two object surfaces, a certain amount of energy is required. A variety of energy sources are available for joining. For nanojoining purposes, the energy source selection is limited due to the extremely small work piece size. Terrones et al. used electron beam irradiation to make "X", "Y" and "T" shape molecular junctions with the covalent cross-linking of C atoms between two crossed CNTs [34]. By placing an individual tube across another one, dangling bonds around vacancies at the contact point can serve as bridges for the merging process. With the help of an electron beam, the junctions made were found to have acceptable quality since atomic bonds were formed and the base materials, CNTs, did not experience much damage in this process. However, the disadvantage was the high cost of operating expensive equipments with complicated procedures.

Hirayama et al. brought straight bundles of CNTs close to other loop bundles of CNTs through a W tip [35]. By slowly increasing the bias voltage, the two bundles touched at one point by electrostatic force with the estimated contact resistance of 100MΩ. An approximate power of 40nW (2v, 20nA) was applied at the contact area to raise the local bundle temperature to an estimated temperature of 3000-4000K although the heat conduction could not be precisely calculated. Since the estimated working temperature was higher than the evaporation temperature of CNTs, it was reasonable to assume that the CNTs experienced structural damage and atom rearrangement which resulted in the joining of the two bundles. Except for the contact

area, other portions of the bundles were not experiencing high temperature, so their structures were probably not visibly changed. Then the joint quality depended on the joint structure; however, it was not examined in detail.

Chen et al. simply left droplets of SWCNTs suspension between two Ti electrodes aligned with the help of DC current [36]. By varying the ultrasonic power, the microstructure of the interface was monitored to propose the mechanism of nano-ultrasonic welding. During the ultrasonic nanowelding, the high frequency ultrasonic power was suggested to soften the metals and caused plastic deformation. Deformation occurred under the clamping stress because of the "acoustic softening effect", thus inducing the SWCNTs to embed into the Ti electrodes forming the Ti_xC intermetallics. The authors observed a substantial decrease of 2t terminal resistance which could be explained by the increases in the effective contact area and the formation of conducting carbides at the contact. The ultrasonic welding provided the electronically well behaved joints with primary bonding through carbide formation. The remaining parts of the CNTs experienced no high temperature treatment which is positive to preserve good mechanical and electrical properties of CNTs. The disadvantages of this process are believed to be high operating cost and high demand for monitoring labour.

Dong et al. reported an interesting nanosoldering strategy, where they utilized CNTs as carriers to carry copper cores inside the tubes [37]. A probe was used to control the precise position of the copper encapsulated CNTs to realize nano-spot welding driven by electro migration with increasing bias at the two ends of CNTs to be soldered. They achieved electrically stable nano-joints with much lower power since the melting temperature for copper at nano scale size was found to be greatly reduced. This was claimed as one of the most potentially useful methodologies to produce copper compatible nano-scale IC circuits. Similar to

14

the situations in the electron beam induced nano spot soldering, most parts of the CNTs preserved their original strength without experiencing detrimental heat treatment. Although the joint quality could be not as high as that produced using high energy induced bonding due to the weak bonding between Cu and CNTs, the lower energy input makes this technology a potential one to be explored. Similar to the nano-soldering idea above, Banhart et al. joined CNTs together through irradiation induced soldering [38]. The hydro carbons absorbed by CNTs from the environment act as the "filler metal" in that work.

Besides direct joining, researchers all over the world have been seeking alternative ways, considering the high difficulty to work on such nano-scale objects. Luo et al. produced 1D heterojunctions of Ni/CNTs and Ag/a-CNTs by using a combined synthesis methods of electrochemical deposition and chemical vapour deposition with improved porous membrane of anodic aluminum oxide (AAO) [39]. The electrical property of 1D Ag/a-CNTs heterojunctions was measured accurately by Atomic Force Microscopy (AFM). This method is universal for producing most 1D amorphous semiconductor and metal nanowires. Thus it was suggested to provide an opportunity for realizing large scale electronic circuitry by precise interconnection among various nano wires and nano tubes through precise growth.

2.2.2 Joining through secondary forces

Dong et al. reported a method to bond the CNTs to a substrate by applying surface clamping force (vdW) to flatten CNTs against the surface, thus promoting a close contact with between the two surfaces [40]. A connection through the secondary force (molecular attraction force) was formed, which proved to be much weaker than the primary bonding. It is thus not widely used for CNTs joining.

Almost all the above nano-joining methods require expensive equipments and have no corresponding equipment for joint quality evaluation. Most of them have focused on CNTs/CNTs joining except for the ultrasonic welding and the Cu soldering. These two approaches focus on the CNTs/metal joining. Ultrasonic welding is a promising approach; however, it suffers limited data on the joint strength evaluation due to the absence of available equipment. The applications of Cu soldering have also been limited by the lack of any joint evaluation technique. Thus a novel approach of CNTs/metal joining with corresponding joint strength evaluation is required.

2.3 Joint quality evaluation

2.3.1 Mechanical characterization

Similar to any macroscopic joints, the evaluation of the nanoscopic joint quality is an essential feedback on the control of the joining process. In macroscopic welding, the joint quality can be always examined through mechanical tests and microstructure analyses of the failure surfaces.

Li et al. have worked on joining the CNTs strands by using epoxy to produce CNTs/epoxy adhesive joints [16]. As shown in **Figure 2.6**, with higher concentration of epoxy soaking solution, lower tensile strength and Young's modulus of the resulting composite fibre were achieved. By employing less concentrated soaking solution which is less viscous, the average tensile strength and Young's modulus (1.5 GPa and 28 GPa) exceeded those of original CNTs strands with values of 1.2 GPa and 16 GPa. Compared to the original strands, the improvement of tensile strength and Young's modulus were 25% and 75%, respectively. The improvement of Young's modulus could be understood since the material was modified by adding epoxy, which

16

makes the fibres stiffer. The improvement of tensile strength was not substantial, which provided further possibility to improve the mechanical property.
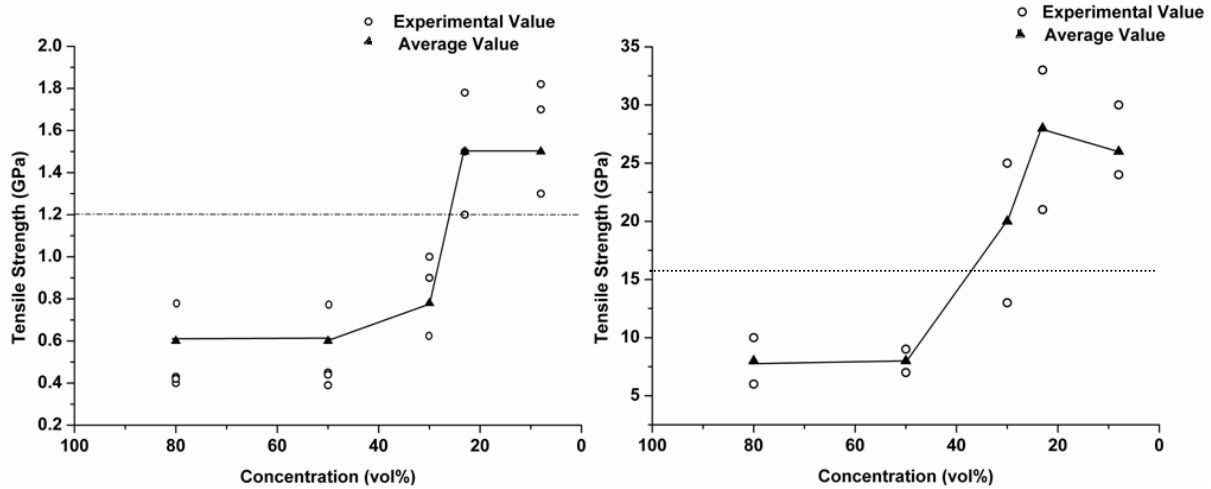
Figure 2.6 Mechanical properties of DWCNTs/epoxy composite fibres at different concentrations of soaking solutions. The dashed lines correspond to the average tensile strength (1.2GPa) and Young's modulus (16GPa) of the original DWCNTs strands. [16]

Gong et al. have also produced epoxy reinforced CNTs joints [41]. The mechanical properties of the joints by adding epoxy are shown in **Figure 2.7**. As the soaking solution concentration of epoxy increased from 0 to 10 vol%, the tensile strength and the Young's modulus were improved by factors of 88% and 83%, respectively. When the concentration increased from 10 to 50 vol%, the tensile strength was not much different from the value at 10 vol%, and the Young's modulus was 143% of the value at 10 vol%. This can be understood in the way that when the soaking concentration increased to a certain value, the improvement of the tensile strength induced by epoxy approached the limit since the epoxy just worked as the medium for transferring the load among the individual tubes. Because the Young's modulus represents the stiffness of a material, it should increase as the concentration gets higher. The

17

joining is achieved only through van der waals force, which indicates that the joint strength is weak. The disadvantage of this joining method is the electrically insulating nature of the epoxy. The adhesive joint is poor in electrical conduction thus not suitable for electronic applications.
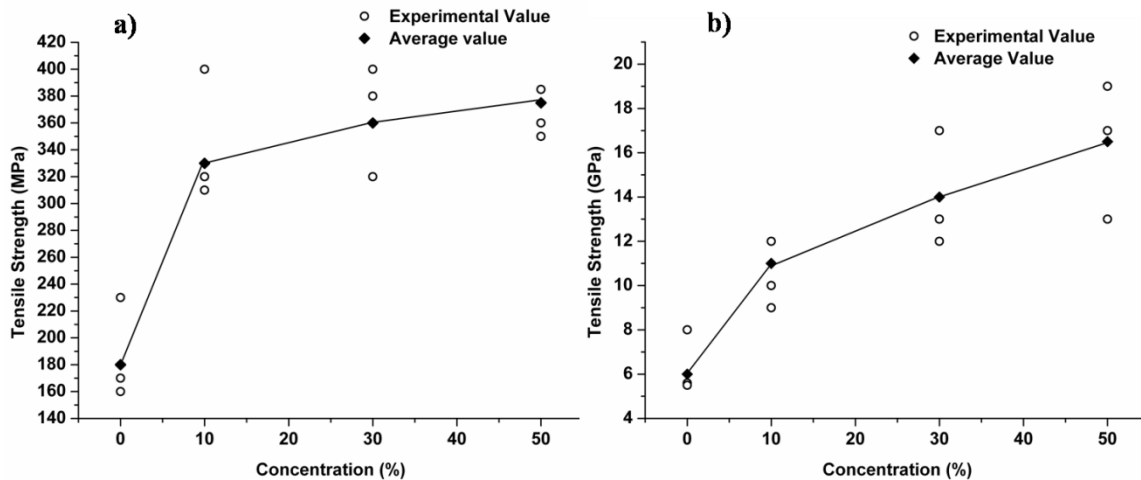
Figure 2.7 Mechanical properties of the composite joints at different concentrations of soaking solutions. [41]

2.3.2 Fracture analysis

Gu et al. were the first to perform tensile tests on CNTs membranes [15]. The SEM images in **Figure 2.8** show the CNTs membrane and the fracture surface after a tensile test. It indicates that individual CNT were not aligned perfectly along one direction within the CNTs membrane, and they were instead tangled together like a web. When the tensile stress was applied, the individual tubes first started to align along the direction of the stress. When the elastic region of the CNTs itself was surpassed, the aligned CNTs strands slipped between each other. The firm junctions of the bundles were firstly torn up then completely detached. It was deduced that the maximum breaking force is a reflection of the van der Waals force between

18

individual CNTs. The long pullouts were seen at the edge of the fracture surface in **Figure 2.8b**, which again confirmed the slippage between adjacent bundles.
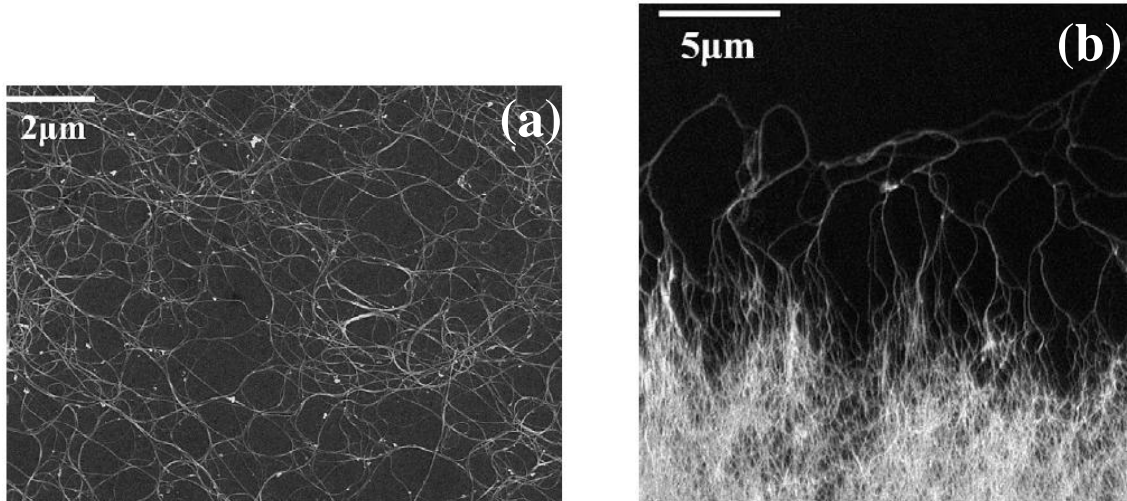
Figure 2.8 (a) SEM of a thin CNTs membrane; (b) SEM of a broken CNTs membrane after tensile test. [15]

Gong et al. [41] used a tensile tester to pull the bandage joined CNTs strands (joint formed between CNTs strands through molecular attraction force) apart and observed the fracture surfaces, as shown in **Figure 2.9**. The main factor affecting the tensile strength of the original joint was the slippage between the overlapped strands bonded through the weak van der Waals force. The CNTs itself did not contribute much to the strength of the joint. Therefore, the bandage joint provided similar strength as the CNTs strands themselves. In order to reinforce the strength of the joint, they produced CNTs/composite joint by embedding CNTs into the epoxy. They compared the original bandage joined CNTs with the joint reinforced with epoxy resin. The original bandage joined CNTs had lower tensile strength than the composite reinforced joints. As shown in **Figure 2.9a,c**, the CNTs/composite joint had a fracture surface very different from bandaged CNTs joint. In the bandaged joint, longer CNTs pull outs were seen protruding out of the fracture surface, which indicates a high degree of slippage. Whereas only short broken CNTs

were seen in the CNTs/composite join leaving a neat and less pulled out fracture surface. Higher tensile strength then resulted. The epoxy itself did not contribute much to the higher strength due to its lower mechanical properties compared to CNTs; however, it acted as an adhesive intermedium to transfer the load between the overlapped CNTs strands. In this case, even though some CNTs were broken during the loading process, the epoxy could still contribute to the final ultimate tensile strength through the interfacial shear strength between CNTs and epoxy.
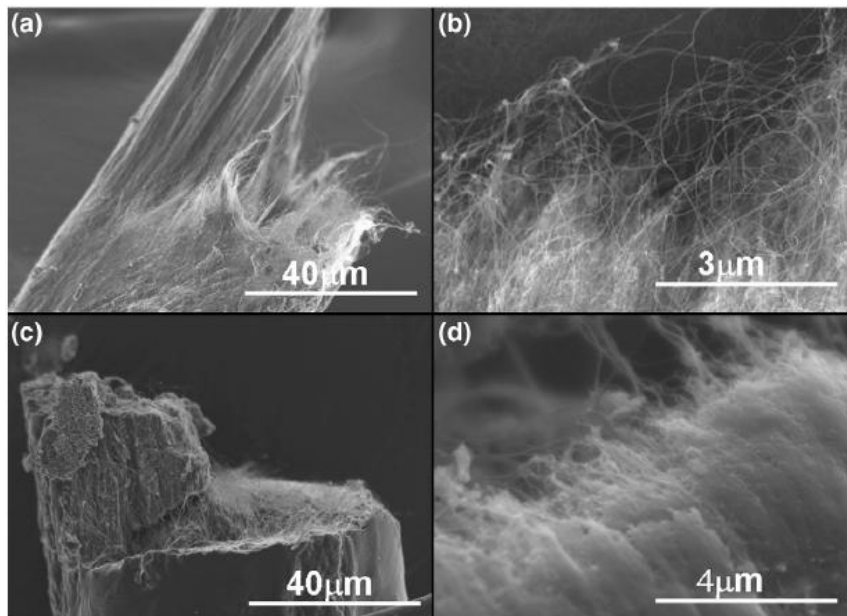
Figure 2.9 (a) An original bandaged joint; (b) high magnification of its local area; (c) composite joint; (d) high magnification of its local area. [41]

Li et al. [16] also conducted tensile tests on the macro-sized DWCNTs/epoxy strands with a length of 10mm and a diameter of 4~35μm and investigated the fracture surface of the pull outs. They claimed that with low soaking concentrations of the epoxy, the pullouts on the fracture surface were longer than the pullouts at a higher soaking concentration. It was concluded that the

lower the concentration of the epoxy, the higher the tensile strength of the joint could be, which

is consistent with Gong et al.'s results [41].

Based on the microstructure studies in the work described above, all the results regarding

the CNTs strand joints obtained showed that the fractures were due to a slippage induced

mechanism. This is considered to be inadequate for practical applications due to the nature of the

weak bonding through van der Waals forces.

2.3.3 Electronic characterization

Table 2.2 Comparison of the resistance of original strands and the strands connected in two different ways. [42]

No.	Resistance (Ω)		
	Original (R1)	Pasted with silver glue (R2)	Bandaged with DWCNTs film (R3)
1	30	26	27
2	34	30	24
3	28	25	22
4	69	60	58.5
5	143.5	118	120.5

Besides the mechanical performance, the electronic performance of the joined CNTs

strands is of great interest too since it directly affects the electronic performance of the joints in

practical applications. Gong et al. [42] have measured the resistances of the bandage joined

CNTs strands, compared to the Ag paste joined CNTs strands, as shown in **Table 2.2**. It was

found that the bandaging joined strands and the Ag paste joined strands had comparable contact

resistance which was even lower than that of the original strands. The decrease in contact

resistance by inducing Ag paste could be understood due to the small resistivity of silver. The

decrease in contact resistance by bandage joining was mainly due to the intensive shrinkage of the CNTs film during the bandaging process where the overlapped strands were compacted together very closely resulting in a lower contact resistance.

The electronic properties of DWCNTs are often evaluated by their resistivity dependence on temperature (R-T curves) [43]. Every R-T curve of DWCNTs exhibits a transition temperature (T*). When the temperature is below T*, the resistivity of the DWCNTs increases as the temperature decreases (like semiconductors); while above T*, the resistivity of DWCNTs gradually increases as the temperature increases (like metal). The lower T* indicates better metallic properties. On the other hand, the electronic property of DWCNTs can also be reflected by the resistivity at room temperature [ρ(RT)], or the ratio of ρ(LT)/ρ(RT) where LT is the lowest temperature during a measurement. When these two values are smaller, better metallic properties are expected [44].
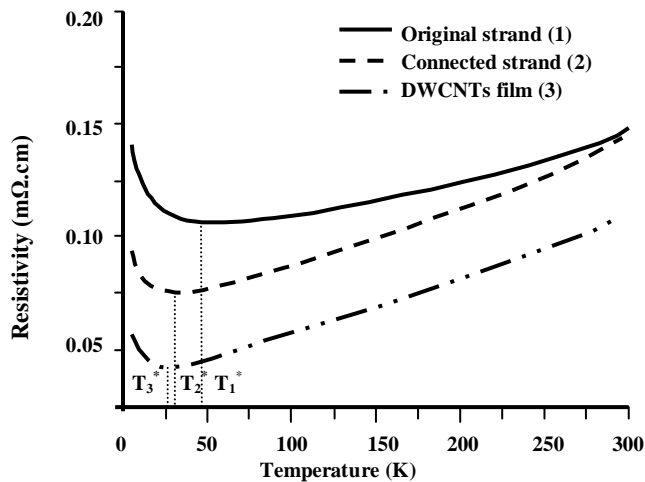
Figure 2.10 The R-T curves of the bandaging connected strand with the original strand and purified DWCNTs film. [42]

Gong et al. have measured and plotted three R-T curves of original DWCNTs strands, bandage joined DWCNTs strands, and the bandaging medium- DWCNTs film, as shown in **Figure 2.10** [42]. The figure shows that the transition temperatures of original strands, connected strands and DWCNTs films decrease in the sequence from 42K, 32K to 27K. The values of $\rho(LT)/\rho(RT)$ also decrease in the same sequence from 0.95, 0.69 to 0.53. It is thus concluded that the increment in metallic properties are in the same sequence. Original DWCNTs strands have more impurities which may be responsible for the higher T*. The joined DWCNTs strands have both T* and $\rho(LT)/\rho(RT)$ very close to the DWCNTs film, however a bit larger. Many factors may lead to the lower T* of DWCNTs films, such as curving, alignment, overlapping and defects inside the DWCNTs films [45]. The film can provide better channels for the electron conduction than joined DWCNTs strands and DWCNTs strands itself.
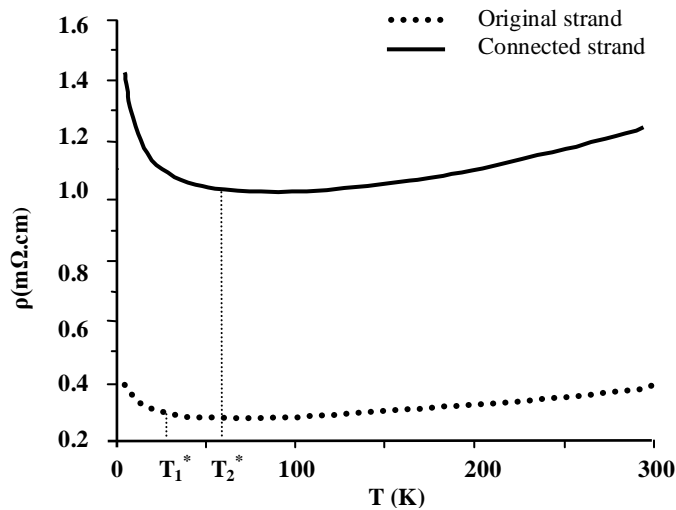
Figure 2.11 The R-T curves of the original strand and the connected strand. [44]

The R-T curve of the DWCNTs strands connected by a bandaging process with laser irradiation enhancement is compared to the one of the original strands shown in **Figure 2.11**[44].

23

After joining, T* of DWCNTs increased from 62 K to 87 K and the ρ(RT) value increased from 0.35 to 1.24 mΩ • cm both of which indicated a reduction in the metallic property after joining. This reduction could be explained by the structural transformation of DWCNTs into multi-walled carbon nanotubes (MWCNTs) due to the laser irradiation. MWCNTs do exhibit worse electronic properties than the DWCNTs. Even so, the ratio of ρ(LT)/ρ(RT) of the joined strand (1.15) was found to be close to that of the original strand (1.02), which means that the main characteristic of the electronic property of the laser enhanced strands did not change, compared to the original strands.

2.4 Lamp application of joining of CNTs strands

Some attention has already been paid to use of DWCNTs strands in practical applications, for example, the DWCNTs filament lamp. Shu et al. produced DWCNTs strands 12mm long, then fixed them onto brackets with Ag paste for the illumination inside a vacuum lamp [46]. The configuration of the DWCNTs filaments is shown in **Figure 2.12** and is compared to that of a tungsten lamp. It is apparently seen the DWCNTs filaments emit stronger light than tungsten filaments.
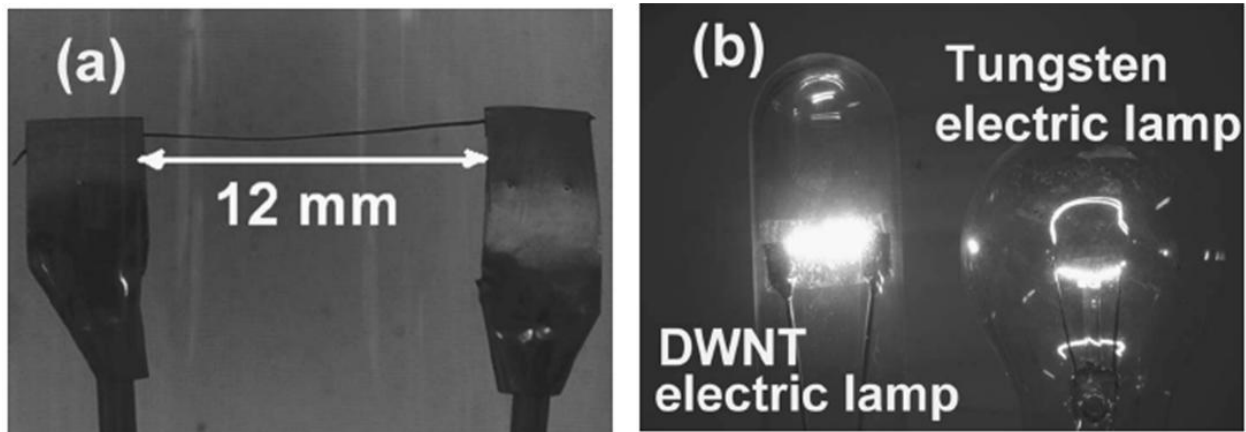
Figure 2.12 (a) A DWNTs filament fixed on brackets; (b) Lighted lamps of DWNTs and tungsten filaments. [46]

The lighting efficiency of the DWCNTs filament is compared quantitatively to the tungsten filament in **Figure 2.13** [46,47]. The efficacies of both lamps with different diameters increased with increasing voltage, as shown in **Figure 2.13a**. The efficacies of DWCNTs increased much faster, which indicated that the DWCNTs lamp had higher efficacy than the tungsten lamp at the same applied voltage. **Figure 2.13b** shows the relative efficacies of both tungsten and DWCNTs filaments increased with increasing input power. For example, the relative efficacy of the DWCNTs electric lamp was 9.1 lx/W at the input power of 40W, while that of tungsten lamps at input powers of 40 and 60 W were about 4.4 and 6.6 lx/W, respectively. The conclusion that DWCNTs filament is superior to the tungsten filament was drawn. Furthermore, after a reliability test of 3000hrs, the electric resistance of the DWCNTs filament decreased from the initial value of 34 to 21Ω. This was due to the high density of spherical amorphous carbon clusters [48] or CNTs junction formation [49] during light emission. However, tungsten filament is proved much more reliable over time.
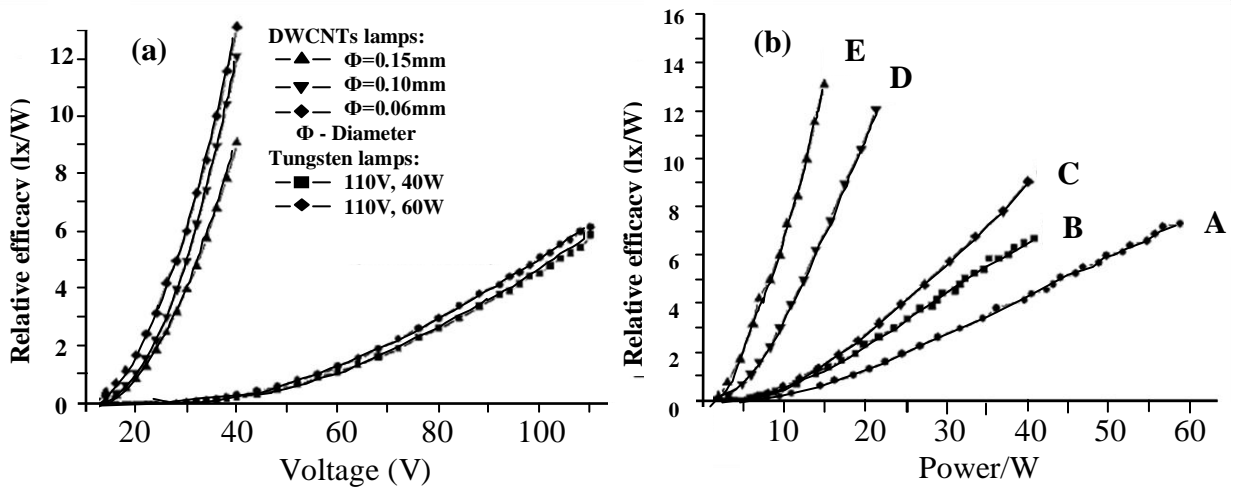
Figure 2.13 Relative efficacies of lamps at different (a) voltage and (b) power. Curves A and B represent tungsten lamps with rated voltages of 110 V, 60 W and 110 V, 40 W, respectively. Curves C, D, and E represent DWNTs electric lamps with filament diameters of 0.15, 0.10, and 0.06 mm, respectively. [46,47]

Diameter ϕ, electric resistance R, current density J, and relative efficacy K_r of the three different DWCNTs filaments at the supply voltage of 40 V are listed in **Table 2.3**. It was found that the relative efficacy of DWCNTs filaments with smaller diameters was higher than that of those with larger diameters. This could be understood from the geometrical dimension aspect. Ugarte et al. showed that the electrical resistivity along the CNTs axis is smaller than the resistivity perpendicular to the axis [50]. Therefore, a conclusion could be drawn that the DWCNTs filaments with smaller diameter should obtain higher current density with the same length, at the same supply voltage.

Since the heat generated per unit volume of the DWCNTs filament increases with the increasing current density, high current density will certainly lead to high temperature on the filament surface. Li et al. reported that the relative efficacy of DWCNTs filaments increased with increasing surface temperature [47].

Table 2.3 The current density and relative efficacy of DWCNTs filaments with different diameters at the voltage of 40 V. [47]

Φ (mm)	R (Ω)	J (A/mm^2)	K_r (lx/W)
0.06	108	32.7	13.2
0.10	76	16.7	12.1
0.15	40	14.1	9.1

Based on the blackbody radiation, a tungsten filament produces only joule heating while the current flows. Unlike a tungsten filament, two different models [51,52,53] have been proposed to explain the DWCNTs radiation: blackbody radiation due to joule heating and

electroluminescence behaviour. Li et al.'s results [47] showed that light emission from DWCNTs filaments is the combination of the blackbody radiation and the electroluminescence. At low voltages, the filament works in the blackbody radiation mode because the energy absorbed by the filament is not high enough to excite the electrons to higher levels. At high voltages, the filaments absorb enough energy to excite electrons up into higher energy levels from which the electrons come back to the lower energy levels. In this process, photon emission occurs, which exhibits higher efficacy than the blackbody radiation. The different illumination behaviours between DWCNTs and tungsten filaments result in the higher efficacy of DWCNTs filaments than tungsten. Moreover, although only DWCNTs filaments were studied, other type of CNTs filaments should also exhibit high efficacies.

2.5 Vacuum brazing

2.5.1 Brazing Fundamentals

Brazing by definition refers to a group of welding processes in which coalescence is produced by heating to suitable temperatures above 450°C (840°F) and by using a ferrous and/or nonferrous filler metal that must have a liquidus temperature above 450°C (840°F) and below the solidus temperature of the base metals, as shown in the schematic diagram of **Figure 2.14**. The filler metal is distributed between the closely fitted base metal surfaces. As temperature increases, the filler metal starts to become molten, and then flows through the gap between the base metals by capillary attraction force until it is evenly distributed, then solidifies between the base metals upon cooling. In principle, there are many energy sources available for brazing, such as torch brazing, furnace brazing, induction brazing, blanket brazing, electron-beam induced brazing, laser brazing and so on. While in this work, furnace brazing was found to be the optimum option

available for engineering consideration due to its comparative high performance to cost ratio. A large volume of furnace brazing is performed in vacuum, which helps to prevent oxidation and often eliminates the need for flux.
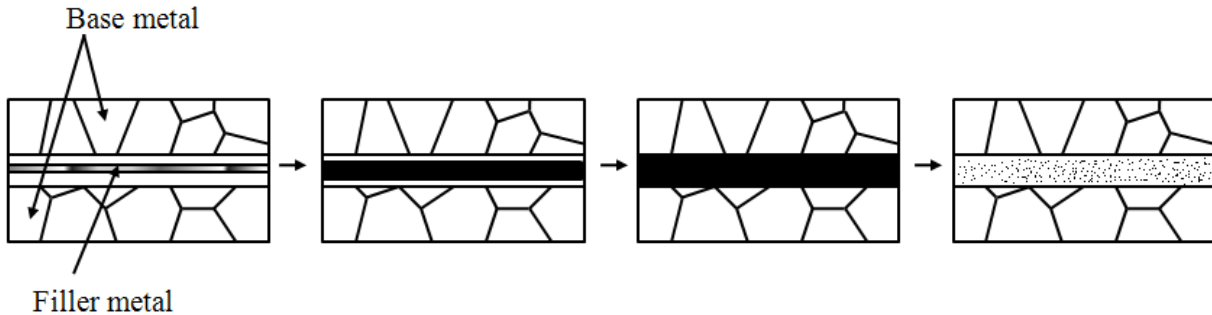
Figure 2.14 schematic of brazing process [54]

2.5.2 Ceramic brazing

Brazing is a promising method to join metallic and non-metallic materials by chemical bonds at interfaces. This method utilizes the wetting action of a molten filler metal and its subsequent solidification. The non-metallic materials and the base metals are connected to a filler metal by covalent bonding and metallic bonding, respectively. Metallic to non-metallic joining will only work if the non-metal surface is able to act as a metal [55]. The brazing of ceramics to each other and ceramics to metals is more difficult since standard brazing alloys are not able to wet ceramics directly. This is due to the significant discrepancy of chemical bonding types—metallic bond on one hand and covalent bond on the other hand. In principle, dissimilar bond characteristics can be transferred to similar bond characteristics through different ways depending on the different types of ceramics (e.g. Al_2O_3, ZrO_2, Si_3N_4, SiC, CFC) [56].

There are two methodological approaches for the brazing of dissimilar materials [55]. First, a one-step brazing procedure uses BFMs which have been alloyed with reactive metallic elements. This direct brazing process is called active metal brazing. The preferred reactive components are the elements from the IVb and Vb groups of the periodic table. These highly reactive elements (Ti, Zr, Cr, Hf, V, Ta or Al) could form e.g. carbides or nitrides at the ceramic/BFM-interface and modify the ceramic surfaces to metalloids which are directly wettable by the remaining BFM. Chromium and titanium are the most effective elements to enable the wetting of carbon materials [5]. The second approach is a two-step procedure, widely used for oxide ceramics like Al_2O_3. During the procedure, the ceramic surface is metalized first and then brazed with a regular non-active filler metal.

During the active metal brazing process, with surface tension modified, different interactions between the base materials and the filler metal take place. These interactions include segregation, grain boundary dissolution, and alloy formation between the filler and the base ceramic. In the case of continuously precipitated intermetallic phases (IP), the joint could be brittle and unreliable, enhancing the risk of fracture. Precipitation of new phases might be at the ceramic/braze interface, in the middle of the joint, or at the BFM/base metal interface, always depending on the thermodynamics of the elements. Some research groups carried out active metal brazing to carbon materials, such as graphite. Gotoh et al. have brazed graphite armor tiles (40 mm x 40 mm x 10 mm) to stainless steel substrates (1 mm thick, 68 mm diameter) with the insertion of copper-carbon fiber composite (Cu-C) layers (1.7 mm thick) [57]. Ag-28 wt% Cu-5wt% Ti BFM and Ag-28wt% Cu BFM were used for brazing the graphite/Cu-C interface and the Cu-C/stainless steel interface, respectively.

2.5.3 CNTs/metal wetting mechanism

Brazing is governed by surface wettability. Surface wettability is characterized by the contact angle between solid and brazing liquid. The contact angle further depends on several factors, including the surface tension of liquid/molten matrix, the surface properties of the CNTs, brazing filler metal and brazing parameters, i.e. temperature, pressure and atmosphere [58,59]. Moreover, the formation of reaction products at the interface plays a critical role in determining the wetting kinetics [60,61].

The interfacial bonding between metal and CNTs has been documented from theoretical and experimental aspects related to reaction product formation. Kuzumaki et al. investigated the wettability of CNTs/Al composite with no reaction product found [62]. They employed Kelly–Tyson's formula to estimate the strength of the composite, however, with discrepancy relative to their experimental results. It was claimed that this discrepancy was a consequence of non-homogeneous dispersion of CNTs in the Al matrix. Laha et al. investigated the interface of CNTs/Al-Si composite with the formation of β-SiC [63]. It was suggested by Laha et al. that from thermodynamic consideration, the Gibbs free energy (-280KJ/mol) of the β-SiC formation was lower than that of Al_4C_3 (-64KJ/mol) thus leading to a higher possibility for the β-SiC formation. It has been observed by Ip et al. that the β-SiC formation improved the wettability of molten Al-Si alloy on graphite surfaces [64]. It was also reported by Laha et al. that the wettability within a solid-liquid-vapour system followed Young's equation (2-2),

$$\cos\theta = \frac{\gamma_{SV} - \gamma_{LS}}{\gamma_{LV}} \qquad (2\text{-}2)$$

where θ is the wetting angle, and γ_{SV}, γ_{SL}, γ_{LV} are the surface energies at different interfaces. S, V and L represent solid, vapour and liquid phases, respectively. At the initial wetting stage, the wetting angle between CNTs and matrix is large, 135-140°. The adhesion between metal and graphite is formed through van der Waals interaction [65]. As the formation of carbide increases, the wetting angle decreases to 55° [66,67].

2.5.4 Parameters

The important factors influencing the quality of brazed joints are materials, heat source, atmosphere, and process. The brazing materials selected in this work are carbon nanotubes (CNTs) strands with the evaporation temperature above 2000°C, Ag based alloy (Ag-63wt %, Cu-35.25wt %, Ti-1.75wt %) as the metallic filler metal with a melting range of 780 °C-810°C and Ni as a base metal. The heat source is chosen to be the high temperature tube furnace (Thermo Scientific Company) which can reach a temperature of 1400°C with a vacuum condition of 10^{-6} Torr. The atmosphere is chosen to be vacuum. The only adjustable factor remaining is the process. The operation of the furnace is limited by the nature of the tube materials so that the preheat process and cooling process are predefined as 2-5°C/min, with the only variable of the temperature control to us. In conventional macro-scale brazing, dissolution rate of base metal in molten filler can be explained by the following equation:

$$dC/dt = K(A/V)(C_s - C) \qquad (2\text{-}3)$$

where, C is the concentration of solute in the liquid after reaction time t, K is a constant, A is the

interface area between the solid and liquid, V is the volume of liquid, and C_s is the saturation concentration of solute in liquid. C_s is dependent on temperature. As the brazing temperature increases, the dissolution of base metal increases, which has an important effect on the joint quality [56].

2.6 Summary

Since CNTs were discovered by Sumio Iijima [1] in NEC, it has become a promising candidate for applications in NEMS. CNTs may provide outstanding mechanical, electrical and thermal properties, such as comparable stiffness as diamond, considerably less resistivity than metal and high thermal conductivity. Moreover, the structural defects of CNTs could be healed by elevated temperature treatment which could form part of a joining process.

Various methods have been tried for joining of CNTs. They are mostly direct nano-joining by employing high energy sources to destroy the intrinsic structure of CNTs thus realizing individual CNTs joining. These complicated procedures suffer the lack of equipment and methods for testing joint quality. Vacuum brazing may be a good approach for CNTs/metal nano-joining based on the macro ceramic brazing.

CNTs macro-strands joining has been attempted, and the mechanical performance of the joint was examined. It has been observed that the ultimate tensile strength (UTS) of the joint could be improved by adding epoxy to the CNTs. The obtained fracture surface microstructure confirms the mechanical performance of the joint. Compared to the original strand, the UTS improvement was 25%. However, the added epoxy is not good for electronic applications.

32

Evaluation of joint quality through UTS is commonly employed, thus it is chosen as the standard to be utilized throughout this study.

Chapter 3

Experimental Details

3.1 Materials chemistry and properties

The carbon nanotube strands (CNTs) used in this study were prepared using a floating catalytic decomposition method as described in Reference [4]. CNTs normally carry a small percentage of Fe catalyst nanoparticles. There is no liquid phase of CNTs, and it will directly evaporate at temperatures above 2000°C. The morphology and structure of the individual tubes in the CNTs strands are shown in **Figure 3.1**. These CNTs strands are typically 30-600 μm wide and several centimetres long. The cross section of the strands shows an oval shape with dimensions of approximately $100\,\mu m \sim 600\,\mu m$ by $13\,\mu m \sim 37\,\mu m$, as measured by SEM examination.

CNTs strands were brazed to two pieces of Ni substrates (0.5 cm x 2 cm x 0.11 mm) which have a melting point of 1455°C. Two pieces of near-eutectic brazing alloy (Ag_xCu_y) foil (0.5 cm x 1 cm x 0.05 mm) doped with active element Ti were used as the brazing alloy to wet CNTs strands at high temperatures under a high vacuum (10^{-6} Torr). The brazing alloy is composed of Ti (1.75 wt.%), Ag (63 wt.%) and Cu (35.25 wt.%). It has a melting range from 780°C to about 815°C. The brazing alloy is commercially available from Morgan Advanced Ceramics Inc. This alloy is typically called active brazing alloy which differs from normal alloys due to the vacant d electron shell of Ti, which may greatly increase the ability of the alloy to react with other non-active materials including ceramics. Within the investigated brazing temperature range (room temperature to 1000°C), only the brazing alloy melts.
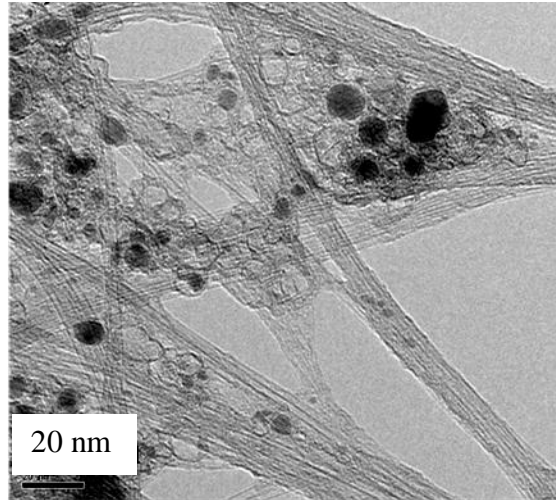
Figure 3.1 TEM image of the as received CNTs strands.

3.2 Brazing procedure

An experimental rig was designed where two pieces of Ni were utilized as the substrates to hold two pieces of Ti-Ag-Cu alloy on the top surfaces. Then one macro-sized CNTs strand was placed onto the top of the alloy pieces, bridging them. The whole rig consisting of the CNTs and the brazing alloy was delivered into a high vacuum tubular furnace, as shown in **Figure 3.2**. The temperature inside the furnace increased slowly with a rate of 2°C/min until the appropriate brazing temperature and stayed at that temperature for 10 minutes. The temperature was then brought down with a slow cooling rate of 2°C/min as well. As a result, the experimental rig was kept in the furnace for around 8 hrs until the furnace temperature reached the brazing temperature (between 850°C to1000°C). It was then kept for 10 mins to allow the flow of the molten alloy and the reaction between alloy and CNTs.

Figure 3.2 The apparatus of vacuum oven used for the vacuum brazing of CNTs strands.

3.3 Tensile test

After vacuum brazing, lap-shear tension testing was performed to characterize the mechanical properties of both CNTs strands and CNTs joints. The tensile tests were conducted with an Instron 5548 micro tester. A schematic diagram of the tensile test set up is shown in **Figure 3.3**. Coupon cross sectional dimension varied from one to another; individual strand dimensions were taken into account when engineering strength was calculated, assuring the comparable and systematic results.
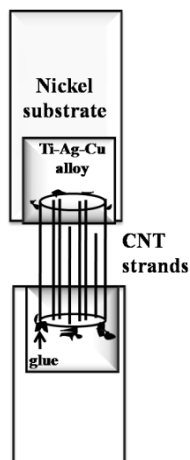
Figure 3.3 Schematic of mechanical tensile test coupons.

There are no standards for the joint quality; however, some groups have utilized ultimate tensile strength (UTS) to evaluate the strength of the joint. In this work, UTS of the joint was calculated based on the joint cross sectional dimensions measured *via* SEM.

3.4 Interface investigation

Although the joints were formed between CNTs and Ni through the Ti-Ag-Cu alloy, the interface of most interest was between CNTs and Ti-Ag-Cu alloy. Therefore, through this work, the CNTs joint is referred to CNTs/Ti-Ag-Cu joint. The cross sectional nano/microstructures of the interface area between the CNTs and the Ti-Ag-Cu alloy were investigated with a LEO 1530 Field Emission Scanning Electron Microscope (SEM) equipped with Energy Dispersive Spectroscopy (EDS), and with a High Resolution Transmission Electron Microscope (HRTEM) Jeol 2010. The cross sections of the joints were cut using a Microtome Diamond knife with a precision piezo control of specimen thickness. The TEM samples were less than 50nm thick. The stoichiometry between the CNTs and the Ti-Ag-Cu alloy was analyzed by X-ray Photoelectron Spectroscopy (XPS) and X-Ray Diffraction (XRD).

Chapter 4

Process Development of CNTs Vacuum Brazing

4.1 Brazing feasibility

4.1.1 Joint morphology
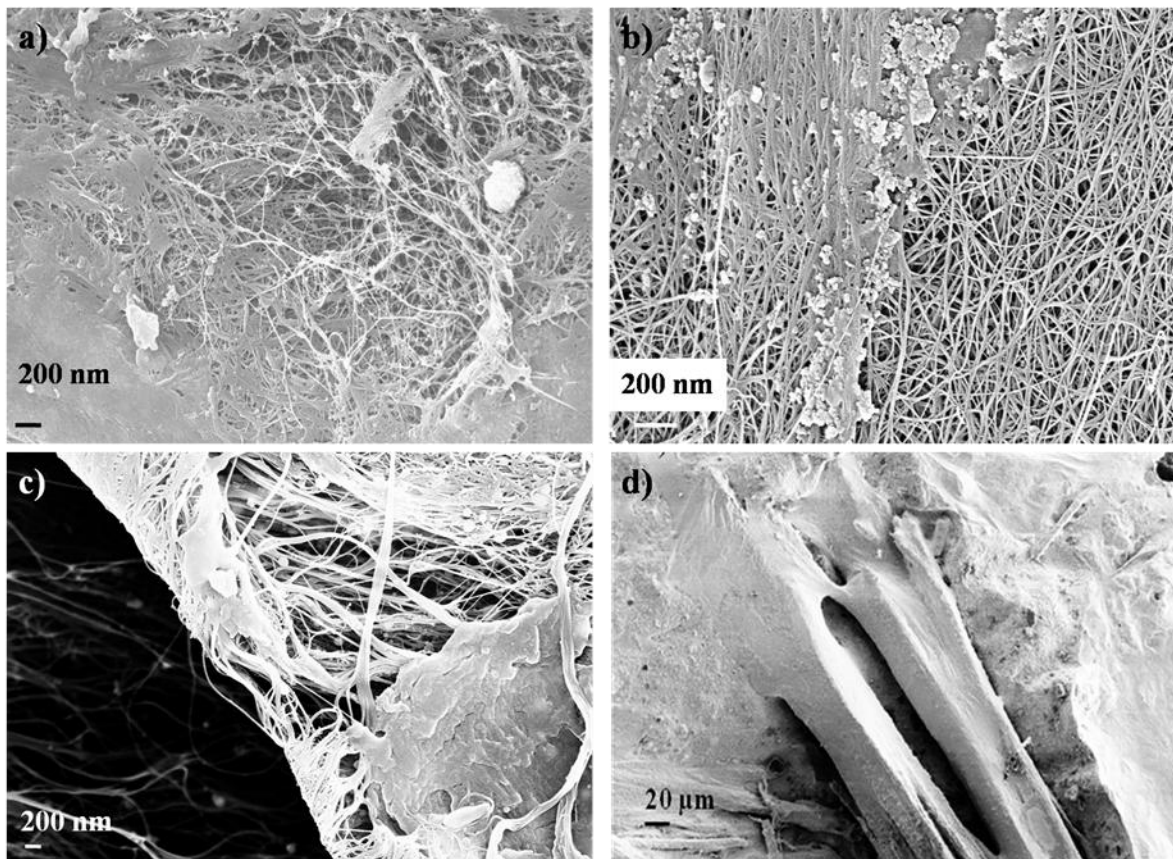
Figure 4.1 (a) SEM image of CNTs brazed with Ti-Ag-Cu alloy at (a) 850 ℃ (b) 900 ℃ (c) 950 ℃ (d) 1000 ℃.

After brazing, the joint morphology obtained at different temperatures is displayed in the SEM micrographs, as shown in **Figure 4.1**. **Figures 4.1a-c** have higher magnification than **Figure 4.1d**. All of the images revealed good wetting where solidified alloy covered the CNTs

tubes surface and even filled in the space in between them. **Figure 4.1d** shows a uniformly brazed alloy which connected two CNTs strands in a very smooth manner. It was observed that the individual tubes in the CNTs strands were embedded into the alloy, indicative of an effective surface wetting. The brazing temperature range (from 850℃ to 1000℃) was found to be sufficient to realize the surface wetting of CNTs. Below 850°C, the brazing alloy did not melt, while above 1000°C, the joints became so brittle that they were fragile upon manipulation.

4.1.2 Mechanical performance of both CNTs and joints

Figure 4.2 shows the tensile test results for the annealed CNTs strands and the brazed CNTs joints from room temperature to 1000°C. Compared to the tensile strength of 189 MPa obtained from SWCNTs strands [16], the as-received CNTs strands in this work only reached an ultimate tensile strength (UTS) of around 25 MPa, as shown in the figure. This discrepancy is believed to be indicative that the present CNTs strands may suffer defects. From RT to 850°C, the UTS value was doubled to around 48 MPa. As the brazing temperature increased from 850°C to 900°C, the tensile strength dramatically increased up to a maximum value of 130 MPa. While from 900°C to 1000°C (the highest temperature investigated), the UTS dramatically dropped to 28 MPa.

Similarly, as brazing temperature increased from room temperature up to 900°C, the UTS of the joints reached a maximum value at 900°C. Namely, below and above 900°C, the joint strength was lower than that at 900°C. During the ex-situ transfer, the joints were frequently observed either not well connected (below 900°C) or brittle (above 900°C).
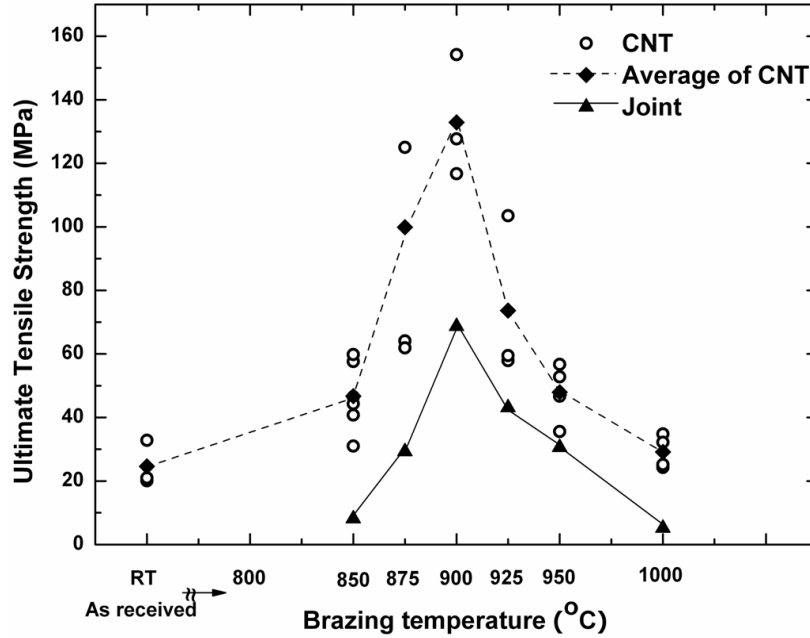
Figure 4.2 Comparison of the joint strength as well as the CNTs mechanical strength.

It was observed that two types of failure occurred for CNTs joints when the UTS was surpassed: the interfacial fracture and the CNTs fracture, as shown in **Figure 4.3b,c**, respectively. Interfacial fracture mainly occurred at the brazing alloy in the joint close to the CNTs side. It was observed that below or at 900°C, the fracture mode was mostly interfacial. The CNTs fracture mainly occurred at CNTs in the joint above 900°C.
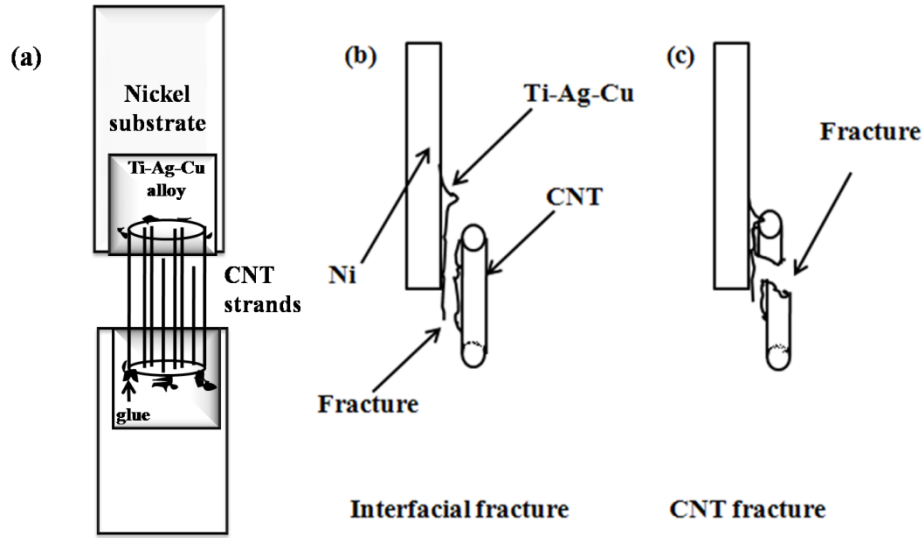
Figure 4.3 a) Schematic of tensile test of specimen; b) Interfacial fracture mode after tensile test; c) CNTs fracture mode after tensile test

4.2 Brazing mechanism

The chemical stoichiometry of the elements in the joint interface brazed at 1000 ℃ was measured through X-ray photoelectron spectroscopy (XPS). Two major peaks shown in **Figure 4.4c** at 532.1 eV and 284.1 eV correspond to oxygen and carbon. The carbon evidently originated from the CNTs. The oxygen peak was believed to come from an amorphous oxide layer covering the surface of the brazed CNTs, which is likely formed during the ex-situ transportation of the CNTs strands to the XPS chamber after vacuum brazing. The Ti peaks observed in **Figure 4.4a** (taken from the joint interface) at 454.9 eV and 461.0 eV, are of good fit with the values of 454.8 eV and 460.8 eV, the characteristic values of Ti $2p_{3/2}$ and Ti $2p_{1/2}$ shells of the Ti-carbide (Ti_xC) crystals [68].
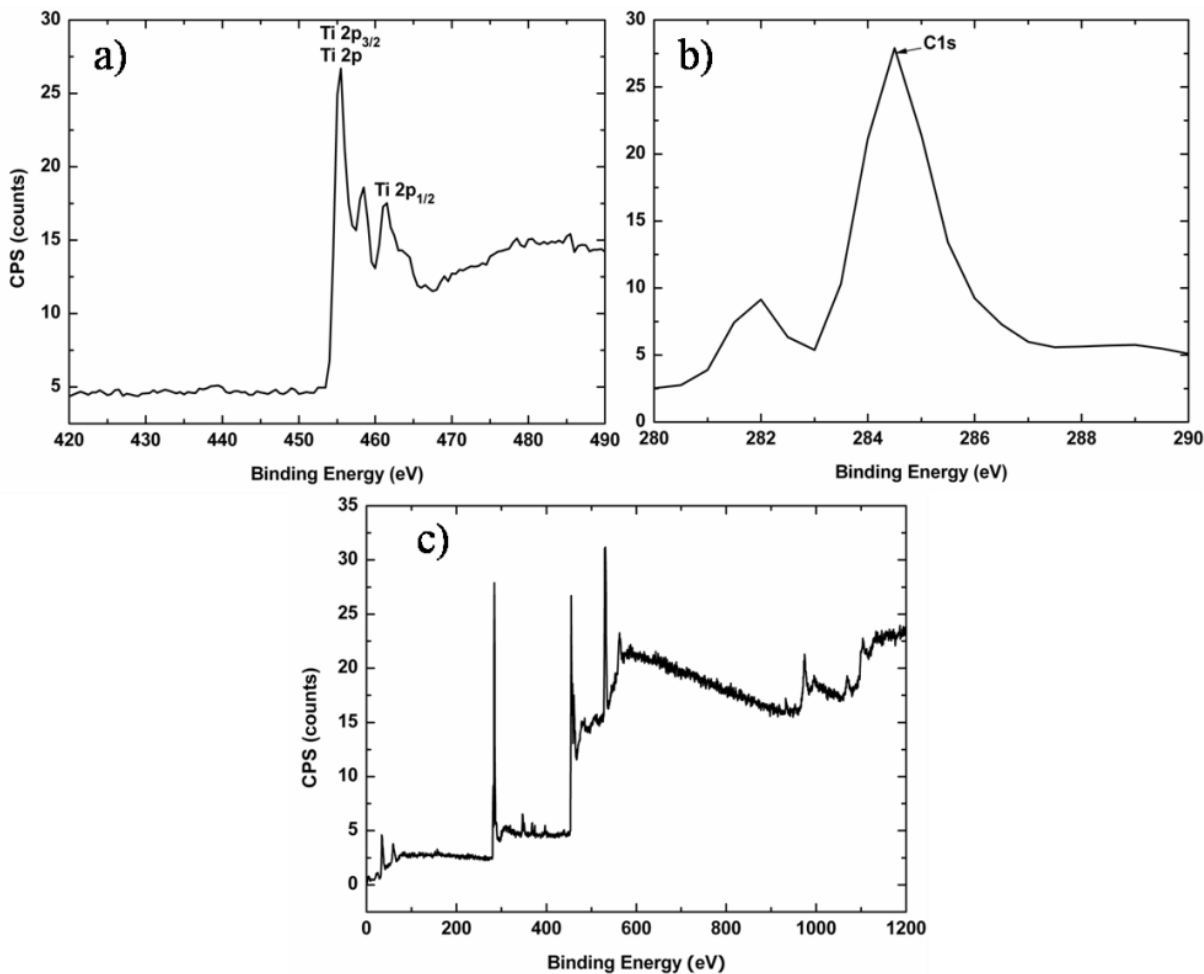
Figure 4. 4 a) XPS spectra near the Ti binding energy of 454 eV on the wetted region of brazing CNTs. b) XPS spectra of C1 s core-level. c) XPS survey spectra.

Additional evidence of the formation of Ti_xC includes the peaks of C 1s at 281.9 eV (**Figure 4.4b**) and Ti 3p at 34.0 eV (**Figure 4.4c**). Those two peaks are close to 281.6 eV and 33.8 eV, the characteristic energy peaks of Ti_xC crystals given in Reference [69]. It should be noted that the C 1s peak of the Ti_xC crystals shifts towards lower energies (281.9 eV) compared to published values of the elemental C 1s level (284.1 eV). This indicates a higher tendency of the formation of covalent bonds between Ti and C atoms due to an increase in the electronegativity of Ti–C bonds. The difference between the values of the energy peaks (281.6

eV) presented in Reference [69] and those found here (281.9 eV) may result from an experimental error. However, it may also be due to the difference in the valence of the Ti cations in the Ti_xC phases. The added (doped) Ti atoms are active elements which are able to form bonds of mixed characteristics with the metal matrix atoms and the covalent hexagonal carbon lattice of the CNTs, which is consistent with the theory proposed by Asthana et al. [59]. The melting and the high temperature of the brazed alloy help to improve the contact of the Ti atoms with the CNTs. This contrasts to the behaviour of solid-state ultrasonic nano-welding of CNTs to Ti [70]. In ultrasonic nano-welding, external forces and ultrasonic energy are required to produce plastic deformation of Ti electrodes to aid the contact between Ti and the CNTs, and to provide energy to the C atoms to covalently bond to the Ti (matrix) atoms. The brazing mechanism is thus further confirmed to be due to the formation of covalent and metallic bonds among Ti and C, and among Ti, Ag and Cu atoms, respectively. The formation of carbide is helpful to reduce the wetting angle thus inducing good surface wetting as found by others [60,61].

4.3 Summary

The vacuum brazing of CNTs strands to Ni through active brazing filler metal Ti-Ag-Cu has been developed successfully, avoiding the difficulty of manipulating individual CNTs. The successful wetting has been confirmed *via* microstructure investigation. The bonding mechanism was confirmed to be due to the formation of TiC. Mechanical performance of both CNTs and joints indicates that temperature imposes significant effects on the joint quality and the CNTs themselves. Investigation of temperature effects on brazing mechanism of CNTs/Ti-Ag-Cu, microstructure and stoichiometry of joints is reported in detail in the next chapter.

Chapter 5

Process Optimization of CNTs Vacuum Brazing

5.1 Microstructure change of CNTs

During brazing, CNTs strands experience annealing which greatly affects their microstructure. HRTEM images of as received and annealed CNTs strands are shown and compared in **Figure 5.1**. The as-received CNTs strands were found to be partially interwoven, with some dispersed amorphous carbon and nanoparticles as indicated by arrows. These nanoparticles have been identified as Fe used for the catalytic growth introduced by Zhu et al. [10]. After annealing at 900°C, surfaces of CNTs became cleaner and smoother due to the vaporization of amorphous carbon and healing of defects. Similar results are reported in the Reference [71], where upon annealing at elevated temperatures, better structured CNTs domains were achieved due to the vaporization of the amorphous carbon and the aggregation of catalytic impurities. Also, according to Bhaleraoa et al. [72], defects inside CNTs strands can be reduced through annealing at a temperature higher than the CNTs formation temperature. The reaction temperature of the CNTs strands utilized in this work is 777°C [13]. Lowest annealing temperature 850°C is higher than the formation temperature. Therefore, it can be concluded that the structure defects and amorphous carbon should be reduced at the temperatures from 850°C to 1000°C. Moreover, the CNTs strands annealed at 1000°C revealed quite different structures compared to those in as-received and 900°C annealed conditions. The CNTs strands annealed at

1000°C were seen to be heavily interwoven. Some portions formed complex web-like structures with scattered catalyst nanoparticles.
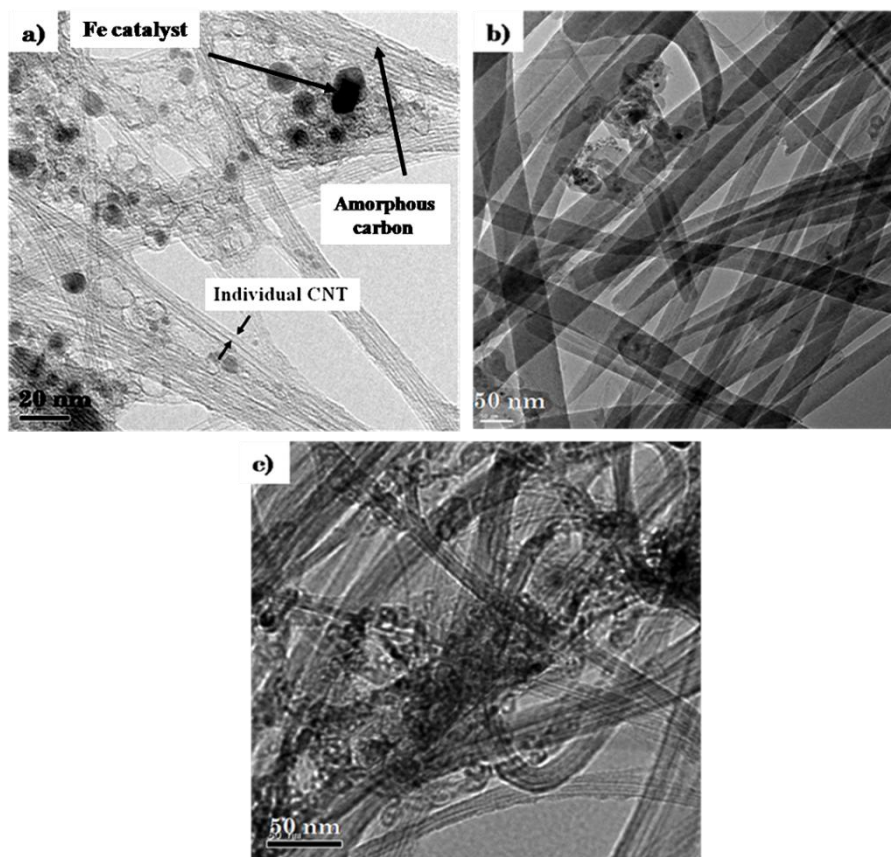
Figure 5.1 HRTEM images of a) as received CNTs; and CNTs brazed at b) 900°C, c) 1000°C.

XRD patterns of the as-received and annealed CNTs strands at 900°C, 950°C, and 1000°C are shown in **Figure 5.2**. A diffraction peak was observed at around 45 deg representing CNTs [73]. Peaks between 15-25 deg mainly came from CNTs [73]. Below 900°C, no peaks assigned to the iron carbide could be found. At 950°C, Fe_4C was identified, and Fe_3C was observed at 1000°C. These results show that iron carbides start to form from 900°C. In this connection, a

similar phenomenon was observed by Ji et al. [74]. They observed that Fe catalyst could be activated above 900°C to react with graphite causing curvature of graphite fibres. This phenomenon was also observed in this work, as shown in **Figure 5.1c,** which appears to confirm the reaction between Fe and C through XRD in **Figure 5.2**.

Although the UTS of CNTs increased as the temperature increased, the heterogeneous distribution of carbide formation above 900°C led to the brittleness of CNTs, which counterbalanced the increment of UTS. As a result, the UTS of CNTs at 900°C was the maximum in this work.
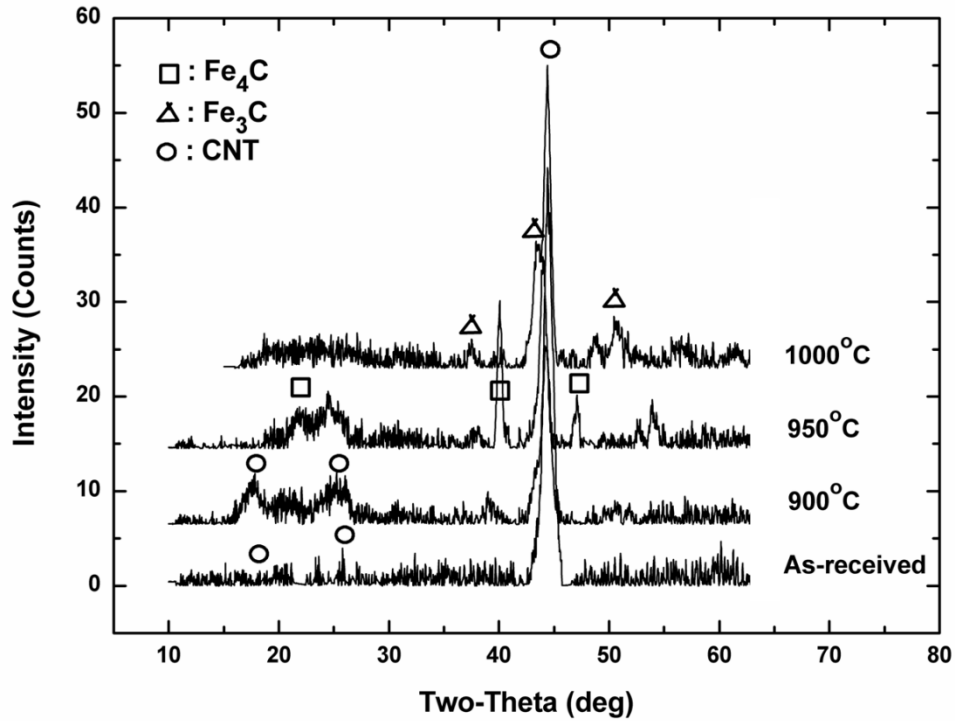
Figure 5.2 XRD of as received and annealed CNTs at 900°C, 950°C, 1000°C

5.2 Fracture analysis of CNTs joints

5.2.1 The stoichiometry change

Temp (°C)	Element (wt%) C	Ti	Fe
850	70	0	18
900	56	1	16
950	61	3	15
1000	29	48	17
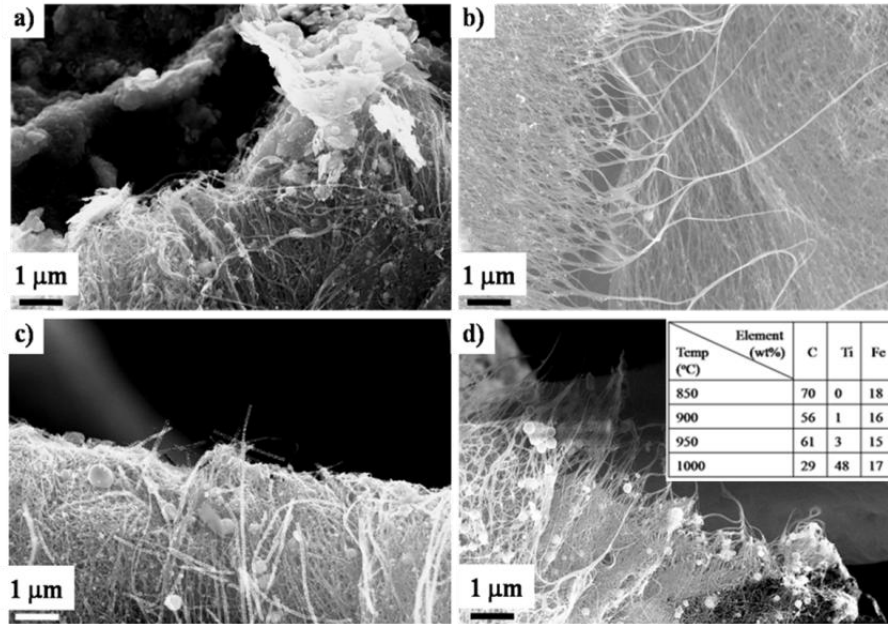
Figure 5.3 SEM images of fracture surfaces of the CNTs joints brazed at a) 850°C; b) 900°C, taken at CNTs side after interfacial fracture shown in Figure 4.3 b); c) 950°C; d) 1000°C taken at broken CNTs remained on the Ti-Ag-Cu alloy after CNTs fracture shown in Figure 4.3 c). Inset: EDX elemental distribution at the fracture surfaces as shown in the a),b),c), d).

Figure 5.3 shows SEM images of the fracture surfaces of CNTs joints brazed at 850°C, 900°C, 950°C, and 1000°C. The interfacial fracture mode (**Figure 5.3a,b**) and CNTs fracture mode (**Figure 5.3c,d**) are illustrated. In order to qualitatively analyze the phase differences in the fracture surfaces, EDX was carried out and the results are shown in **Figure 5.3d inset,** where the test data are summarized in the table. The C concentration decreased to less than half of the

original amount as temperature increased from 850 ℃ to 1000°C. Below 900°C Ti was found in trace amount (around 1%) at the joint area. It is evident that Ti concentration at the joint area dramatically increased above 950°C, especially at 1000°C. The overall content of Fe (catalytic particles) remained almost unchanged. The EDX results indicate that below 900 ℃, little Ti segregates from the brazing alloy into the joint area, while above 900 ℃, more Ti is found in the joint area.
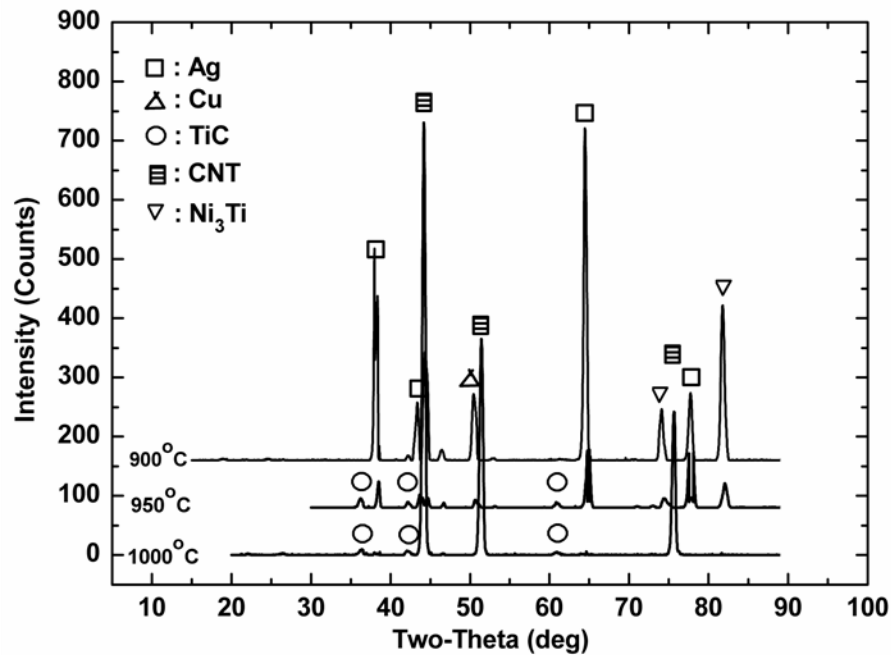
Figure 5.4 XRD pattern of CNTs joints at 900 ℃, 950°C and 1000°C. XRD is taken at Ti-Ag-Cu/Ni side after interfacial fracture at 900 ℃ as shown in Figure 4.3 b), at CNTs/Ni side after CNTs fracture at 950 ℃ and 1000 ℃ samples as shown in Figure 4.3 c) respectively.

The phases at the joint area were further identified by XRD. Since there was not a large difference of the XRD peaks between 900 ℃ and 850°C, only patterns obtained at 900°C, 950°C, 1000°C are illustrated. **Figure 5.4** shows that little TiC was identified at the brazing alloy side at

900°C. At 900 ℃, little CNTs residue was observed on the brazing alloy side after fracture. That allowed sufficient signals from Ag, Cu and Ni$_3$Ti in the XRD pattern. At 950°C and 1000°C, TiC was identified at the brazing alloy side with CNTs residue, indicative of significant TiC formation at the CNTs joint area. This is in good agreement with the EDX results. At 950 ℃ and 1000 ℃, less Ag, Cu and Ni$_3$Ti peaks were found. Based on the SEM-EDX and XRD results, it is believed that, until 900 ℃, little TiC is formed at the joint area and much more TiC is formed at 1000 ℃.

5.2.2 The microstructural changes
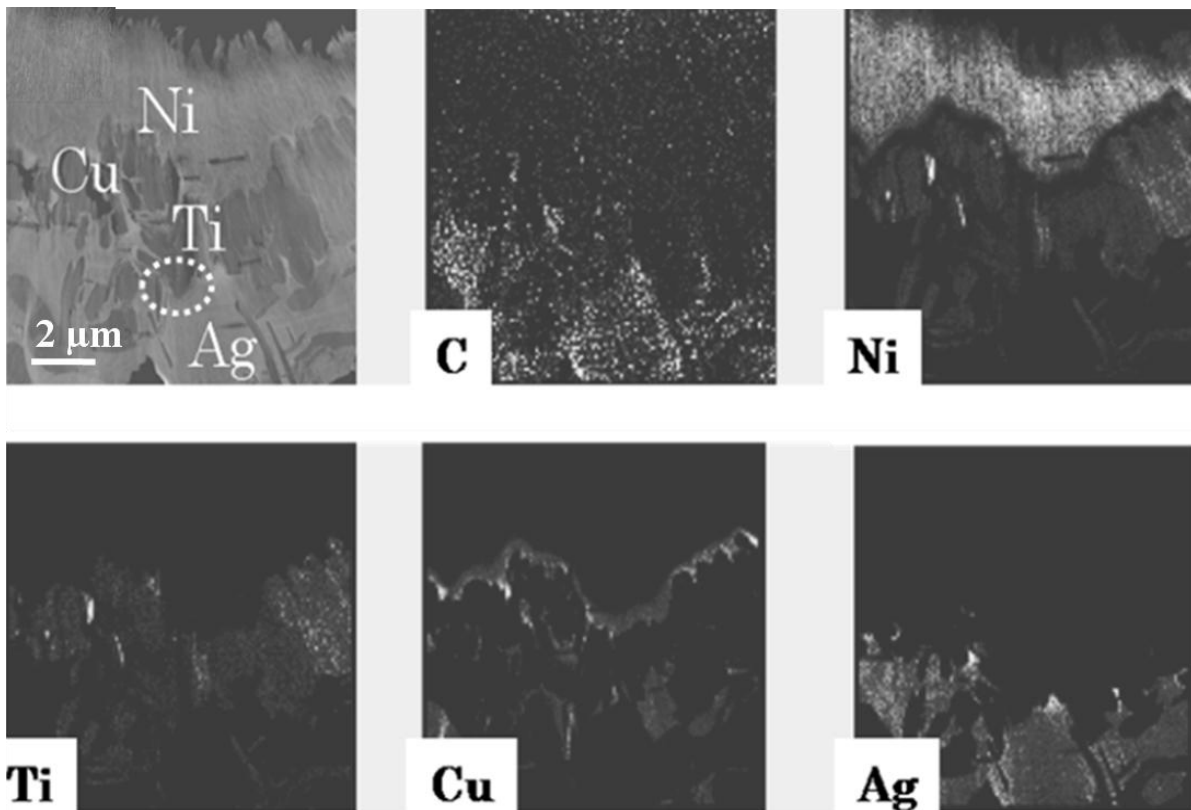
Figure 5.5 STEM elemental maps of interface of CNTs/alloy bonds brazed at 900°C.

The temperature effect on the brazing mechanism was further investigated through TEM. **Figure 5.5** displays an STEM image of a joint interface at 900°C as well as the EDX elemental mapping conducted on the same area. The enrichment of elements is reflected by the contrast in the mapping image. As shown in **Figure 5.5**, Ni appearing in the interface was from the work pieces. Below Ni, Cu traces were found followed by Ti and C. Ag was enriched further away from Ni. It should be remembered that Cu and Ag are the main elements in the brazing alloy while Ti is the minor ingredient. Nevertheless, Ti plays a crucial role in the CNTs joining. Ag and Cu act as carriers to bring Ti close to the CNTs strands [6].
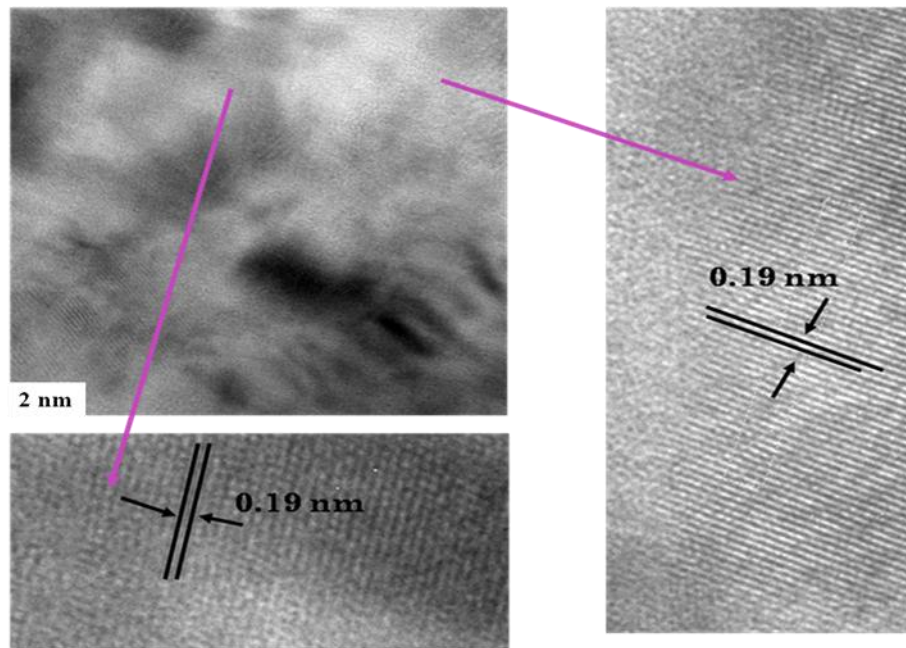
Figure 5.6 Magnified TEM image of Ti/CNTs interface brazed at 900°C.

Figure 5.6 shows an enlarged image of the area highlighted by the circle in **Figure 5.5** to reveal the phase within the interfacial area between C and Ti. There was no TiC formation according to previous XRD and EDX results. Additional work was done to further confirm whether TiC existed at the interface, because the TiC formation may greatly strengthen the joints. Thus the interface between C and Ti is of great interest. The image scanning was conducted at several spots across the interface to ensure representative images could be obtained. At these spots scanned, only similar fringes with the spacing of around 0.19 nm were found (where fringes refer to regularly spaced array). The fringe of 0.19 nm spacing corresponds to Ag (200). No fringes with spacing corresponding to TiC were found. Combined with EDX and XRD results, it is reasonable to believe that TiC exists in a tiny amount, thus making it hard to detected.

Figure 5.7 presents HRTEM images of the interfaces obtained at 950°C. The microstructure of 950°C was found to be quite different from that of 900°C. **Figure 5.7a** shows that numerous CNTs were joined to the brazing alloy (black area), which indicates that the CNTs structure had not been severely damaged at 950°C. Further information regarding the composition at the interface was revealed through the EDX spectrum in **Figure 5.7b**. By employing EDX to search for the highest Ti peak, the area with enriched Ti was located and labelled with a circle in **Figure 5.7a**. The C concentration in this area was also relatively high considering the extremely small sample thickness. Thus this area became the spot of interest.
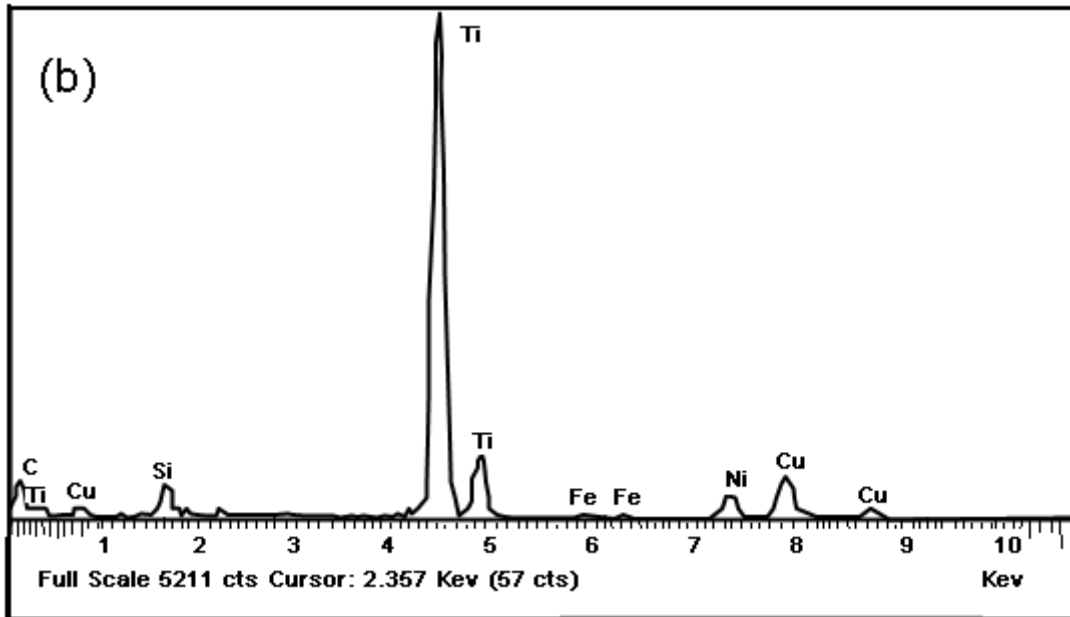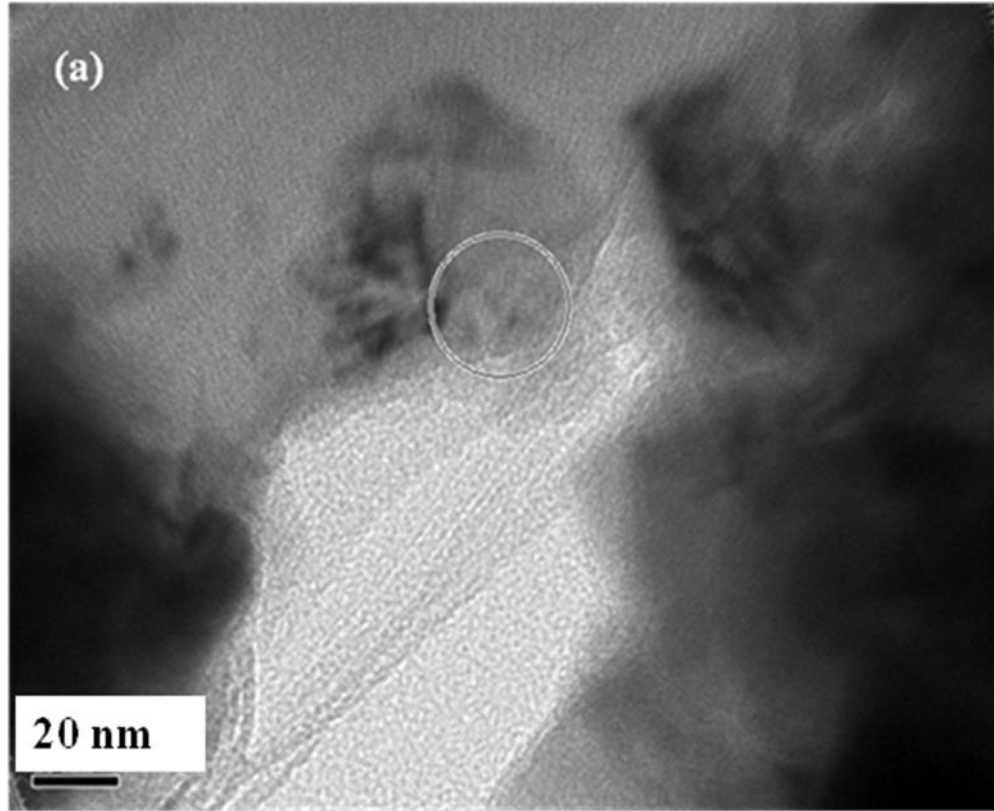
Figure 5.7 (a) TEM image of interface brazed at 950°C; (b) EDX reveals composition at interface.

Figure 5.8a shows a similar microstructure to that in Figure 5.7a, however, taken at a different spot which again was chosen to be representative. It was then decided to take further lattice measurements to identify possible intermetallic TiC formation as already indicated in the XRD pattern. As the area was studied with a higher magnification, it was easy to find fringes with similar spacing of 0.218 nm while differently orientated, as shown in Figure 5.8b. Based on a crystal structure database, the fringe with lattice spacing of 0.218 nm was identified as cubic TiC (200) phase.
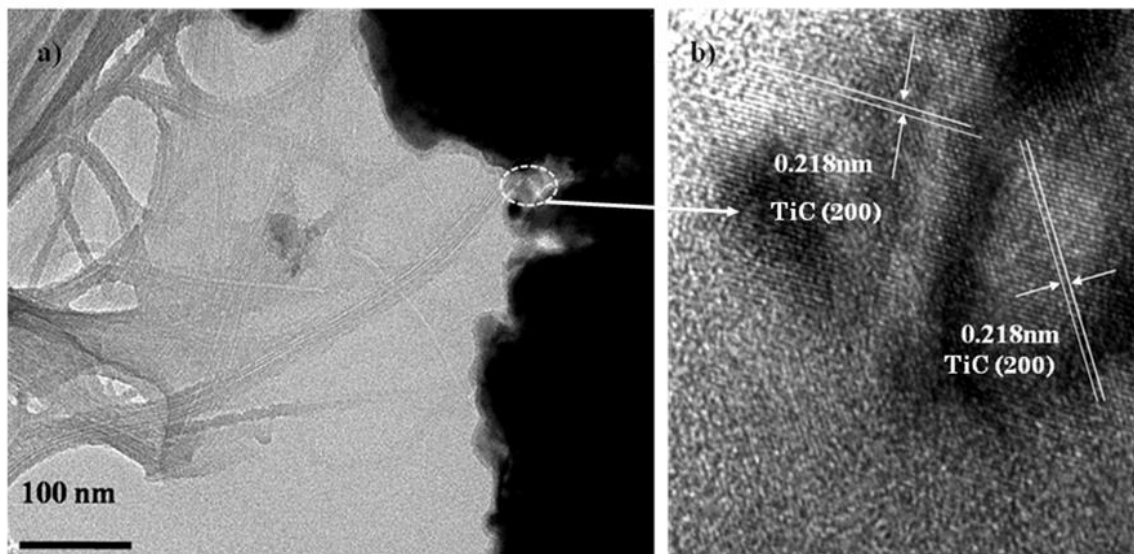
Figure 5.8 (a) TEM images of interface at 950°C; (b) Magnified image of circle in (a) showing fringes.

The cross sectional image of the interface, brazed at 1000°C and cut in situ by the focused ion beam (FIB), is shown in Figure 5.9. The microstructure at 1000°C was quite different from that at 950°C, where no apparent tube-like features were found at 1000°C. Five EDX elemental

phase maps are also presented, corresponding to O, C, Ti, Ag, and Cu, respectively. It was evident that oxygen spread evenly all over the region, which indicates a lack of a preferential oxide layer in the brazed area. A cross in the SEM image was placed at the periphery of the black region. Accordingly, in the Ti and C elemental maps, the cross locates at the edge of the region rich in both Ti and C. It indicates a possible spot for intermetallic TiC formation.
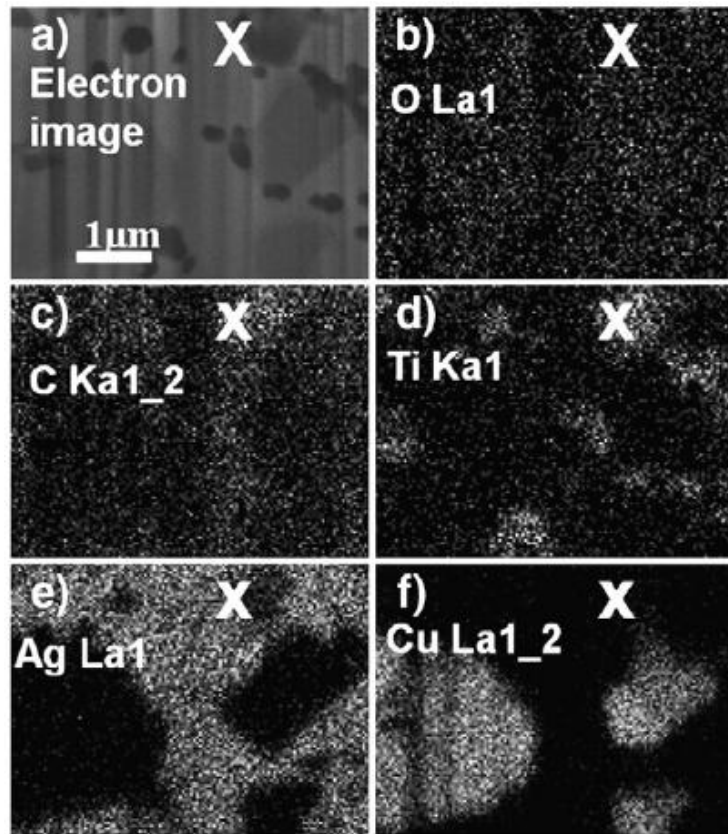
Figure 5.9 Cross section view of (a) CNTs joint area at 1000°C and corresponding EDX element mapping (b–f) of the area with FIB-SEM.

The area including the cross in **Figure 5.9** was further investigated by HRTEM, as shown in **Figure 5.10**. There were no apparent CNTs features identified at 1000°C indicating that more severe CNTs structural damage occurred at 1000°C than at 950°C. Several spots in this area

were discovered with different fringe spacing. These fringes should represent different intermetallic phases among Ag, Cu and Ti. In this area, the only fringe which could be assigned to TiC was the one with spacing of 0.248 nm identified as TiC (111) phase. Such TiC (111) phase was revealed at several spots which indicates the TiC formation commonly occurs. Such a result is in good agreement with the XRD pattern taken at the CNTs joint obtained at 1000°C.
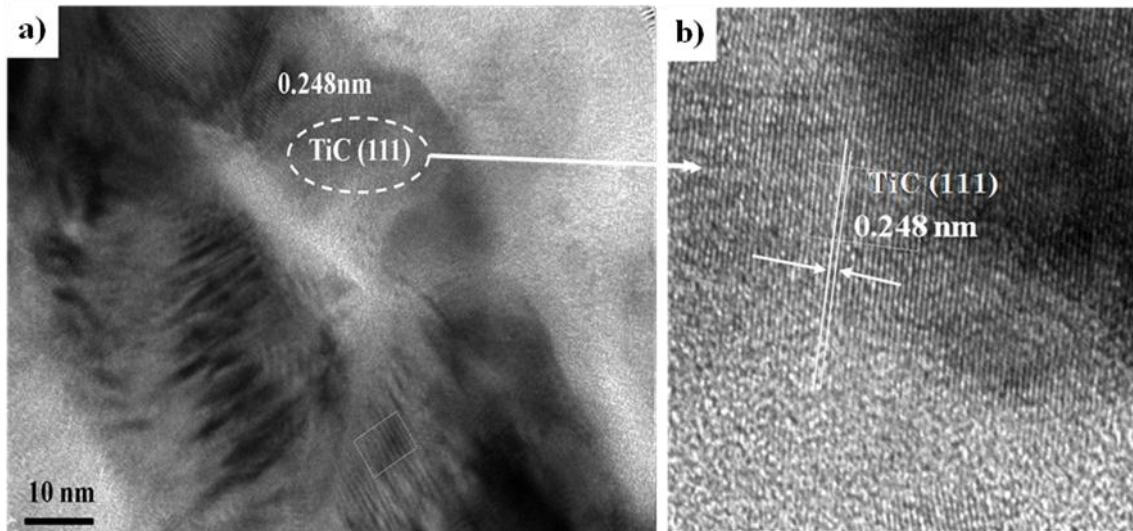
Figure 5.10 HRTEM images of interface brazed at 1000°C.

5.3 Thermodynamic analysis

According to Laha's theory [63], wettability is influenced by the nature of reaction at the interface of CNTs and metallic matrix. Reactions at the interface reduce the wetting angle [63]. A low contact angle indicates a good wettability. From the thermodynamics' point of view [63], the driving force for a reaction to occur arises from the change of Gibbs free energy, $\Delta G = -nFE$ where ΔG is the change of Gibbs free energy, n is the electron number within this reaction, F is

the Faraday constant, E is the electromotive force (EMF). The Gibbs free energy has to be negative for the reaction to occur. The larger the absolute value of the Gibbs free energy is, the more viable the reaction is. Consequently, a large positive EMF means that the reaction is viable. In the brazed joint, possible elements to react with C are Ti, Ag, Cu and Fe. Fe is the catalyst for growth of CNTs. Since the direct measurement of EMF for the reactions between metals with C is difficult, the values can be estimated by simulating other experimental values. For example, the energy released from the combination of Ag^+ and an electron is roughly equal to the energy cost for an Ag atom to lose one electron by omitting the kinetic energy. Similarly, the formation energy of CH_4 can be expressed as the energy released from the combination of one C atom, four protons and four electrons. From these two reactions, we can approximately obtain the EMF value for the reaction of Ag with C. As accurately measured from previous experiments [63], the standard electrode potential (SEP) for Ag and C are 0.7996V and 0.13V, respectively. Combining (5-1) and (5-2), we get (5-3)

$$Ag^+ + e^- \rightarrow Ag(s) \text{ (SEP 0.7996V)} \qquad (5\text{-}1)$$

$$C(s) + 4H^+ + 4e^- \rightarrow 4CH_4(g) \text{ (SEP 0.13V)} \qquad (5\text{-}2)$$

$$4Ag + C \rightarrow Ag_4C \text{ (SEP 0.13-0.7996=-0.6696V)} \qquad (5\text{-}3)$$
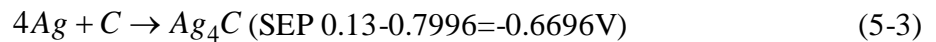
where the EMF for this reaction is -0.6696V.

For the reaction of Ag and C, the negative EMF leads to a positive change of Gibbs free energy, which indicates the reaction between Ag and C is very difficult. The same theory applies to Cu (SEP=0.520V) and the corresponding ΔG is positive as well. Ti is different from Ag and

56

Cu, with SEP=-1.63V which leads to a negative ΔG. The negative Gibbs energy should results in an easier reaction between Ti and C. According to this estimation, Fe catalyst embedded in our CNT samples also easily reacts with carbon atoms.

5.4 Fracture mechanism analysis

As shown above, the as-received CNTs strands consist of randomly aligned tubes with coated amorphous carbon, embedded defects and nano-sized Fe catalyst particles. The strands are virtually entangled networks. As temperature approaches 900°C, the amorphous carbon gradually evaporates, and the Fe catalyst is not activated yet. Meanwhile, the structural defects can gradually be healed, thus the UTS of CNTs increases. However, as the temperature goes beyond 900°C, Fe catalyst starts to be activated. Iron carbides, such as Fe_4C, Fe_3C, are formed at 950°C and 1000°C, respectively. Although the elevated temperature will help remove the structural defects of CNTs, supposedly resulting in higher UTS, the extensive and non-homogenous growth of brittle carbide plays a detrimental role in counterbalancing the healing effect and eventually reduces the UTS.

The joints exhibit a similar trend of UTS versus brazing temperatures, where 900 ℃ is the optimum temperature. As the temperature goes beyond the melting range (780 ℃-810 ℃) of the brazing alloy, more Ti can react with the CNTs. As observed, below 900 ℃, the fracture mode is interfacial fracture, and the UTS of the joint increases as that of CNTs increases until the maximum at 900°C. This is due to the removal of structural defects in the CNTs and the beginnings of TiC formation at the joint interface based on the above results. Below 900 ℃, the joint is weak due to little TiC formation at the joint interface.

In contrast, above 900 ℃, the fracture mode is fracture in the CNTs. Fe catalyst particles originally embedded inside the CNTs strands now become activated and start to form Fe_3C and Fe_4C, which breaks some of C-C bonds. Meanwhile, additional titanium segregates towards the CNTs through the help of molten Ag and Cu matrix. The formation of TiC induces strong bonding at the joint interface. On the other hand, the formation of TiC, Fe_3C and Fe_4C at the CNTs in the joint weakens the CNTs by forming a C- carbides composite material because non-homogeneous dispersion of the brittle carbides lowers the UTS of CNTs [60]. The fracture thus occurs at CNTs in the joint rather than at the interface.

5.5 Summary

Based on the experimental results, it was determined that the UTS of both CNTs and joints achieved the maximum values at 900 ℃. The brazing mechanism was confirmed to dependent on the TiC formation at the interface. Extent of reaction of Ti with CNTs highly depends on the temperature. Below 900 ℃, due to limited TiC formation, the joint strength is weak thus resulting in interfacial fracture. Above 900 ℃, due to the extensive amount of TiC formation at the joint, the joint strength is strong. However, because non-homogenously distributed brittle carbides (Fe_3C, Fe_4C and TiC) are formed, the CNTs portion in the joint, as the weakest part, becomes the fracture surface. Therefore, it can be concluded that 900 ℃ is the optimum temperature for the vacuum brazing process of CNTs. The comprehensive study of temperature effect on CNTs and CNTs joints provides a foundation for future applications or process improvements.

Chapter 6

Application of Brazed CNTs as Lamp Filament

6.1 Experimental setup

The behaviour of the CNTs strands brazed at 1000 °C as incandescent lamp filaments was investigated by placing specimens inside a vacuum chamber (10^{-4}Torr), as shown in **Figure 6.1a**. The CNTs filaments were illuminated, as shown in **Figure 6.1b**. The two contact wires of the experimental lamps were led *via* the feed through on the chamber lid to the DC power supply. For comparison, additional lamps were made just by squeezing CNTs filament between the Ni contact wires, or by Ag paste connection between the CNTs filament and the Ni contact wires, respectively. The I-V curves were recorded during each illumination. The I-V data were read directly through the DC power supply.
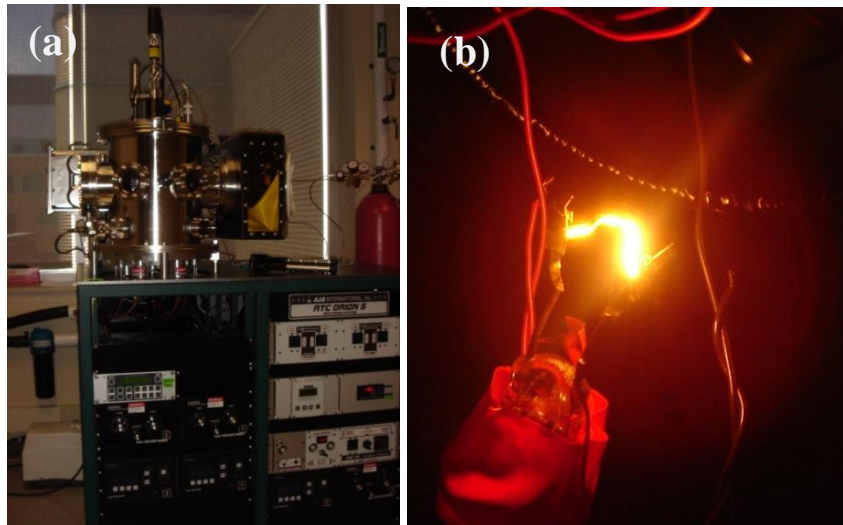

Figure 6.1 (a) Vacuum chamber for CNTs filament application, (b) Illuminating CNTs filament in the vacuum.

6.2 Performance of CNTs filament

Figure 6.2 shows the I-V curves for mechanical squeeze connected, Ag paste connected and brazing connected filaments. Before brazing, the resistance of the filament by mechanical squeezing was large (~514.4Ω), and unstable due to the poor contact. In strong contrast to the resistance of the filament assembly without brazing, the resistance after brazing was dramatically reduced to ~54.8Ω and reasonably stable. With the Ag paste connection, the resistance was ~154.65Ω, higher than the brazing connected filament. Considering the size consistency of the CNTs filament used here, the difference in the intrinsic resistance of CNTs filaments was negligible. Thus it was reasonable to conclude that the dramatic decrease in the brazed filament resistance could be attributed to the decrease of the contact resistance due to the successful brazing. Based on the diameter of the strands and the I(V) curves, the current density of the same filament before brazing, with Ag glue connection and after brazing at applied voltage of 25 V are calculated to be $3.62 \times 10^6 A/m^2$, $1.31 \times 10^7 A/m^2$ and $3.41 \times 10^7 A/m^2$, respectively. Note that Shu et al. [46] measured the current density of a CNTs filament at 40V to be 1.41×10^7 A/m^2 with the Ag paste connection to the substrate. In our experiment, even at a lower bias of 25 V, the brazed filament had a comparable current density with Shu's. Therefore, it can be concluded that the brazing technique dramatically increases the current density of CNTs filaments at the same applied voltage. Since a superior charge transporting capacity up to ~10^{13} A/m^2 has been reported previously in MWCNTs, there is still a large margin to optimize the present CNTs filaments.
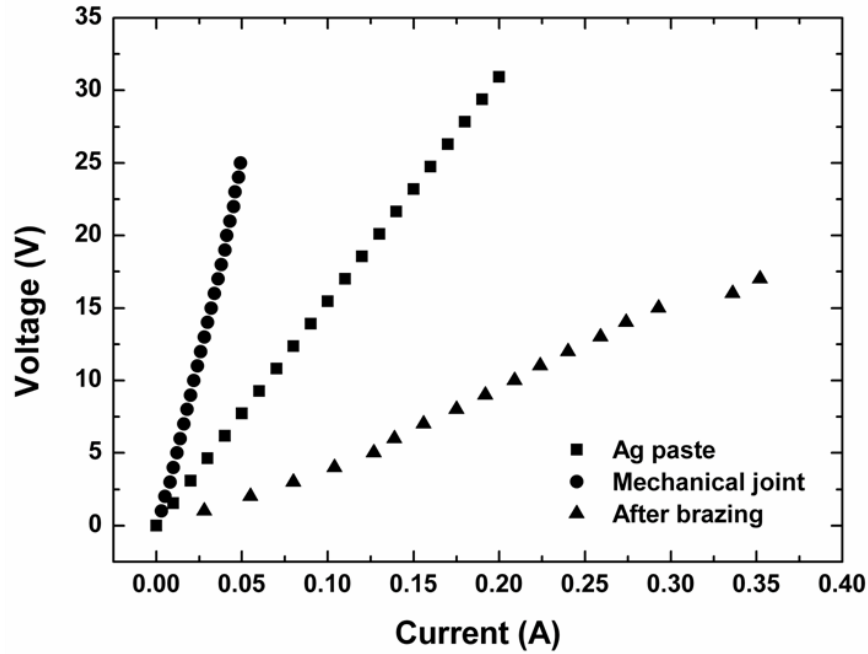
Figure 6.2 I-V curve of the CNTs filaments before and after brazing in comparison with Ag paste connection and mechanical squeeze connection.

6.3 Summary

A vacuum brazed CNTs filament was utilized in an experimental incandescent lamp. The electrical resistance of the filament was measured to be ~54.8Ω, substantially lower than that of one without brazing (~514.4Ω), which indicated that the contact resistance was greatly reduced by brazing. The current density has been measured to be $3.62 \times 10^6 A/m^2$, $1.31 \times 10^7 A/m^2$ and $3.41 \times 10^7 A/m^2$ for CNT filaments before brazing, with Ag glue connection and after brazing at the applied voltage of 25 V, respectively. The superiority of the vacuum brazing technique for filament connections was evident.

Chapter 7

Conclusions

7.1 Brazing process and bonding mechanisms

Based on the experimental results, nanoscale joining of CNTs to Ni *via* vacuum brazing with brazing alloy Ti-Ag-Cu has been successfully developed. The technique is applicable in a temperature range from 850 ℃ to 1000 ℃. The basis for successful nanoscale brazing between the CNTs strands and the brazing alloy is the formation of strong covalent Ti–C bonds. The brazing mechanism has been investigated through TEM, XRD and XPS techniques. The vacuum conditions are essential to reduce the rate of unwanted reactions with oxygen and effectively promote the bonding between Ti and C atoms. The active element Ti acts as the electron reservoir required to form the metallic bonds among the atoms of the metal matrix and the covalent bonds for CNTs strands to be welded.

7.2 Temperature effects

The mechanical performance of CNTs and CNTs joints, and the brazing mechanism have been investigated from room temperature to 1000°C. It was observed that the UTS of both CNTs and the joints achieved maximum values at 900 ℃. The brazing mechanism has been confirmed to be the formation of TiC at the interface. Below 900 ℃, due to the little TiC formation, the joint strength is weak, thus resulting interfacial fracture. Above 900 ℃, due to the extensive TiC formation, the joint strength is high. Due to the brittle carbides formed (Fe_3C, Fe_4C and TiC), the portion of CNTs in the joint is the weakest point and becomes the fracture surface for the CNTs joint assemblies. As a result, it is concluded that 900 ℃ is the optimum temperature for the

62

vacuum brazing process of CNTs. The comprehensive study of the temperature effect on CNTs and CNTs joints provides a foundation for future applications and process improvements.

7.3 Application for vacuum brazing

The vacuum brazing technique to join CNTs to Ni was applied in an incandescent lamp application where CNTs was utilized as a filament. Compared to the filaments without brazing, the lighting efficiency was visibly higher. As calculated, the resistance of the filament before brazing ($\sim$514.4 Ω) is one order of magnitude higher than that after brazing ($\sim$54.8 Ω) and less stable upon measurement. In addition, the current density of the same filament before and after brazing at the applied voltage of 25 V was calculated to be $3.62 \times 10^6 A/m^2$ and $3.41 \times 10^7 A/m^2$, respectively. Compared to the results reported by Shu et al. [46] who measured the current density of CNTs at 40V to be 1.41×10^7 A/m^2 with the Ag paste joining, the current density ($3.41 \times 10^7 A/m^2$) of vacuum brazed CNTs filament is still higher even at a lower supplied voltage of 25V. An energy-saving incandescent lamp with CNTs filaments is thus promising via brazing.

References

1   S. Iijima, **Nature**, 354 (1991) 56.

2   M. T. Martnez, Y. C. Tseng, N. Ormategui, I. Loinaz, R. Eritja and J. Bokor, **Nano Letters**, 9 (2009) 530.

3   M. S. Fuhrer, J. Nygård, L. Shih, M. Forero, Y. G.Yoon and M. S. C. Mazzoni, **Science** 176, 288 (2000) 494.

4   J. Q. Wei, L. J. Ci, B. Jiang, Y. H. Li, X. F. Zhang, H. W. Zhu, C. L. Xu and D. H. Wu, **Journal of Materials Chemistry**, 13 (2003) 1340.

5   Y. Zhou, **Microjoining and Nanojoining**, Woodhead Publishing In Materials, Cambridge, England, (2008).

6   W. Wu, A. M. Hu, X. G. Li, J. Q. Wei, Q. K. Shu, K. L. Wang, M. Yavuz and Y. N. Zhou, **Materials letters**, 62 (2008) 4486.

7   H. W. Kroto, J. R. Heath, S. C. O'Brein, R. F. Curl and R. E. Smalley, **Nature**, 318 (1985) 162.

8   S. Iijima and T. Ichihashi, **Nature**, 363 (1993) 603.

9   T. Erik, Thostenson, Z. Ren and T. Chou, **Composites Science and Technology**, 61 (2001) 1899.

10   H. W. Zhu, C. L. Xu, D. H. Wu, B. Q. Wei, R. Vajtai and P. M. Ajayan, **Science**, 296 (2002) 884.

11   J. Q. Wei, J. L. Sun, J. L. Zhu, K. L. Wang, Z. C. Wang, J. B. Luo, D. H. Wu, and A. Y. Cao, **Small**, 2 (2006) 988.

12   Y. H. Li, Y. M. Zhao, M. Roe, D. Furniss, Y. Q. Zhu, S. Ravi. P. Silva, J. Q. Wei, D. H. Wu, and C. H. Patrick Poa, **Small**, 2 (2006) 1026.

13   Zhu H W, Xu C L, Wu D H, Wei B Q, Vajtai R and Ajayan P M, **Science**, 296 (2002) 884.

14   Y. J. Li, K. L. Wang, J. Q. Wei, Z. Y. Gu, Zhicheng Wang, Jianbin Luo and Dehai Wu, **Carbon**, 43 (2005) 31.

15   Z. Y. Gu, K. L. Wang, J. Q. Wei, C. G. Li, Y. Jia and Z. C. Wang, **Carbon**, 44 (2006) 3315.

16   Y. J. Li, K. L. Wang, J. Q. Wei, Z. Y. Gu, Q. K. Shu, C. G. Li, W. X. Wang, Z. C. Wang, J.

    B. Luo and Wu D H, **Carbon**, 44 (2006) 176.

17   L. M. Ericson, H. Fan, H. Q. Peng, V. A Davis, W. Zhou, J. Sulpizio, Y. H. Wang, R. Booker, J. Vavro, C. Guthy, N. G. Parra-Vasquez, A. Myung Jong Kim, S. Ramesh, R. K. Saini, C. Kittrell, G. Lavin, H. Schmidt, W. W. Adams, W. E. Billups, M. Pasquali, W. F. Hwang, R. H. Hauge, J. E. Fischer and R. E. Smalley, **Science**, 305 (2004) 1447.

18   L. Song, L. Ci, L. Lv, Z. P. Zhou, X. Q. Yan, D. F. Liu, H. J. Yuan, Y. Gao, J. X. Wang, L. F. Liu, X. W. Zhao, Z. X. Zhang, X. Y. Dou, W. Y. Zhou, G. Wang, C. Y. Wang and S. S Xie, **Advanced Materials**, 16 (2004) 1529.

19   X. F. Zhang, T. V. Sreekumar, T. Liu and S. Kumar, **Journal of Physical Chemistry B**, 108 (2004) 16435.

20   R. Saito, M. Fujita, G. Dresselhaus, and M. S Dresselhaus, **Applied Physical Letter**, 60 (1992) 2204.

21   J W. G. Wildöer, L. C. Venema, A. G. Rinzler, R. E. Smalley and C. Dekker, **Nature**, 391 (1998) 59.

22   A. Thess, R. Lee, P. Nikolaev, H. Dai, P. Petit, J. Robert, C. Xu, Y. H. Lee, S. G. Kim, A. G. Rinzler, D. T. Colbert, G. E. Scuseria, D. Tomanek, J. E.Fischer and R. E. Smalley, **Science**, 273 (1996) 483.

23   T. W. Ebbesen, H. J. Lezec, H. Hiura, J. W. Bennett, H. F. Ghaemi and T. Thio, **Nature**, 382 (1996) 54.

24   M. Kociak, A.Yu. Kasumov, S. Guéron, B. Reulet, I. I. Khodos, Yu. B. Gorbatov, V. T. Volkov, L. Vaccarini and H. Bouchiat. **Physical review letters**, 86, 11 (2001) 2416.

25   Z. K. Tang, L. Zhang, N. Wang, X. X. Zhang, G. H. Wen, G. D. Li, J. N. Wang, C. T. Chan and P. Sheng, **Science**, 292 (2001) 2462.

26   S. Berber, Y. K. Kwon and D. Tománek, **Physical Review Letters**, 84, 20 (2000) 4613.

27   P. M. Ajayan and S. Iijima, **Nature**, 361, 28 (1993) 333.

28   X. K. Wang and R. P. H. Chang, **Journal of Materials Research**, 9, 6 (1994) 1578.

29   H. Kataura, Y. Kumazawa, Y. Maniwa, I. Umezu, S. Suzuki, Y. Ohtsuka and Y. Achiba, **Synthetic Metals**, 103 (1999) 2555.

30   J. Kotakoski, A. Krasheninnikov, and K. Nordlund, **Physical Review B**, 74 (2006) 245420.

31   P. Lambin, A. Fonseca, J. P. Vigneron, J. B. Nagy, and A. A. Lucas, **Chemical Physics Letters**, 245 (1995) 85.

32   J. T.H. Tsai and A. A. Tseng, **Journal of Experimental Nanoscience**, 4 (1) (2009) 87.

33 Q. M. Gong, Z. L, Y. Wang, B. Wu, Z. Y. Zhang and J. Liang, **Materials Research Bulletin**, 42 (2007) 474.

34 M. Terrones, N. Grobert, J.-C. Charlier, H. Terrones and P. M. Ajayan, **Physical Review Letters**, 89, 7 (2002) 075505.

35 H. Hirayama, Y. Kawamoto, Y. Ohshima and K. Takayanagi, **Applied Physics Letters**, 79 (2001) 1169.

36 C. X. Chen, L. J. Yan, E. S-W Kong and Y. F. Zhang, **Nanotechnology**, 17 (2006)   2192.

37 L. X. Dong, X. Y. Tao, L. Zhang, X. B. Zhang and B. J. Nelson, **Nanoletters**, 7 (2007) 58.

38 F. Banhart, **Nanoletters**, 1 (2001) 329.

39 J. Luo and J. Zhu, **Nanotechnology**, 17 (2006) S262.

40 L. X. Dong, F. Arai and T. Fukuda, **IEEE Transactions on Mechatronics,** 9 (2004) 350.

41 T. Gong, Y. Zhang, W. J. Liu, J. Q. Wei, Y. Jia, K. L. Wang, D. H. Wu and M. L. Zhong, **Materials Letters**, 62 (2008) 4431.

42 T. Gong, Y. Zhang, W. J. Liu, J. Q. Wei, C. G. Li, K. L. Wang, D. H. Wu and M. L. Zhong, **Carbon**, 45 (2007) 2235.

43 T. Gong, Y. Zhang, W. J. Liu, J. Q. Wei, K. L. Wang, D. H. Wu and M. L. Zhong, **Journal of Laser Applications**, 20 (2008) 122.

44 J. Q. Wei, H. W. Zhu, B. Jiang, L. J. Ci and D. H. Wu, **Carbon**, 41 (2003) 2495.

45 A. B. Kaiser, G. Düsberg and S. Roth, **Physical Review B**, 57 (1998) 1418.

46 Q. K. Shu, J. Q. Wei, K. L. Wang, C. G. Li, Y. Jia and D. H. Wu, **Journal of Applied Physics**, 101 (2007) 084306.

47 C. G. Li, K. L. Wang, J. Q. Wei, B. Q. Wei, H. W. Zhu, Z. C. Wang, J. B. Luo, W. J. Liu, M. X. Zheng and D. H. Wu, **Chinese Science Bulletin**, 52 (2007) 113.

48 Z. G. Zhao, F. Li. C. Liu and H. M. Cheng, **Journal of Applied Physics**, 98 (2005) 44306.

49 S. Agrawal, M. S. Raghuveer, R.Kroger and G. Ramanath, **Journal of Applied Physics**, 100 (2006) 094314.

50 W. A. deHeer, W. S. Bacsa, A. Chatelain, T. Gerfin, R. Humphrey-Baker, L. Forro and D. Ugarte, **Science**, 268 (1995) 845.

51 P. Li, K. L. Jiang, M. Liu, Q. Q. Li, S. S. Fan and J. L. Sun, **Applied Physics Letters**, 82 (2003) 1763.

52 M. Sveningsson, M. Jönsson, O. A. Nerushev, F. Rohmund and E. E. B. Campbell, **Applied**

Physics Letters, 81 (2002) 1095.

53   J.-M Bonard, T. Stöckli, F. Maier, W. A. de Heer and A. Châtelain, **Physical Review Letters**, 81 (1998) 1441.

54   **ASM handbook**, Vol. 6, Welding, Brazing and Soldering (1993).

55   Mel M. Schwartz, **Brazing**, ASM International, Metals Park, Ohio, United States (1987).

56   Mel M. Schwartz, **Ceramic Joining**, ASM International, Materials Park, Ohio, United States (1990).

57   Y. Gotoh, H. Okamur, S. Itoh, T. Wada and Y. Karatsu, **Fusion Engineering and Design,** 9 (1989) 295.

58   R. Andrews and M.C. Weisenberger, **Current Opinion in Solid State and Materials Science**, 8 (2004) 31.

59   R. Asthana, **Metallurgical and Materials Transaction A**, 25A (1994) 225.

60   T. Laha and Y. Liu, A. Agarwal, **Journal of Nanoscience and Nanotechnology**, 7(2) (2007) 515.

61   W. X. Chen, J. P. Tu, L. Y. Wang, H. Y. Gan, Z. D. Xu and X. B. Zhang, **Carbon**, 41 (2003) 215.

62   T. Kuzumaki, K. Miyazawa, H. Ichinose and K. Ito, **Journal of Materials Research**, 13 (9) (1998) 2445.

63   T. Laha, S. Kuchibhatla, S. Seal, W. Li and A. Agarwal, **Acta Materialia**, 55 (2007) 1059.

64   S. W. Ip, R. Sridhar, J. M.Toguri, T. F. Stephenson and A.E.M.Warner, **Materials Science Engineering A**, 244 (1998) 31.

65   J. T. Davies and E. K. Rideal, **Interfacial phenomena**, Academic Press, New York (1961) P34.

66   S. Kalogeropoulou, C. Rado and N. Eustathopoulos, **Scripta Materialia**, 41 (1999) 723.

67   K. Landry, S. Kalogeropoulou and N. Eustathopoulos, **Materials Science Engineering A**, 254 (1998) 99.

68   K. F. Huo, Y. M. Hu, Y. W. Ma, Y. N. Lü, Z. Hu and Y. Chen, **Nanotechnology** 18 (2007) 1.

69   S. V. Didziulis, J.R. Lince, T. B. Stewart and E. A. Eklund, **Inorganic Chemistry,** 33 (1994) 1979.

70   C. X. Chen, L. J.Yan, E. S.-W Kong and Y. F. Zhang, **Nanotechnology,** 17 (2006) 2192.

71   L. J. Ci, Z. Y. Ryu, N. Y. Jin-Phillipp and M. Ruhle, **Acta Materialia**, 54 (2006) 5367.

72   G. M. Bhaleraoa, A. K. Sinha and V. Sathe, **Physica E**, 41 (2008) 54.

73   A.Y. Cao, C. L Xua, J. Liang, D. H. Wu and B. Q. Wei, **Chemical Physics Letters**, 344 (2001) 13.

74   X. L. Ji, H. P. Subramanya, Y. Rho and L. F. Nazar, **Chemical Materials**, 19 (2007) 374.